Journal of Materials Chemistry A

FEATURE ARTICLE

View Article Online
View Journal | View Issue

Cite this: J. Mater. Chem. A, 2014, 2, 7637

Functionalized mesoporous structured inorganic materials as high temperature proton exchange membranes for fuel cells

San Ping Jiang*

Received 8th January 2014
Accepted 28th January 2014

DOI: 10.1039/c4ta00121d

www.rsc.org/MaterialsA

There are significant technological and economical advantages for operating a proton exchange membrane fuel cell (PEMFC) at temperatures above 100–150 °C. One of the key components in the development of high temperature PEMFCs is the proton exchange membrane (PEM). The PEM not only needs to be highly stable in the harsh chemical and physical environment in fuel cells, but also needs to possess high proton conductivity at elevated temperatures and under low humidity conditions. In this paper, the research activity and progress in the development of high temperature PEMs will be briefly reviewed but the main emphasis will be on the development of unsupported and functionalized nano and mesoporous structured inorganic materials such as TiO_2, Fe_2O_3, Al_2O_3 and SiO_2 as high temperature PEMs for fuel cells. Among various inorganic proton conducting materials, heteropolyacid (*e.g.*, $H_3PW_{12}O_{40}$ or HPW) functionalized mesoporous silica, HPW–*meso*-silica, shows particularly promising potential as new PEMs for fuel cells. The challenge and prospects of the development of functionalized mesoporous silica based PEMs for fuel cells operated at high temperatures (300–450 °C) are discussed.

1. Introduction

Among various fuel cells, proton exchange membrane fuel cells (PEMFCs), where chemical energy of fuels such as hydrogen, methanol and ethanol is directly converted to electrical energy, provide an efficient alternative to standard internal combustion engines and are most suitable for applications ranging from portable electronic devices and vehicle transportation to stationary power generation.[1–3] PEMFCs have the advantages of high power densities, very low greenhouse gas emissions, low-temperature operation, rapid start-up and shut-down times, the ability to use fuels from renewable sources, compact design and lightweight.[4–6]

One of the key components in a fuel cell system is the proton exchange membrane (PEM). The state-of-the-art PEMs are perfluorosulfonic acid (PFSA) based polymers like Nafion due to their good mechanical properties, excellent chemical and physical stability and relatively high proton conductivity under fully hydrated conditions.[7,8] However, the water uptake and consequently the proton conductivity of PFSA-based membranes decrease considerably at elevated temperatures (≥100 °C) due to the dehydration and degradation of the membranes over 100 °C and at low relative humidity (RH) environments.[9–13] This loss of conductivity is related to their inability to retain water at high temperatures. The limited operating temperature range complicates water and heat management, requires high-purity hydrogen to avoid CO poisoning of the catalysts and slows down the electrochemical reactions at electrode/membrane interfaces.[14–16] Polymeric membranes are also susceptible to deformation due to the volumetric changes on the basis of adsorption/desorption of water. The deformation increases the electrode/membrane interface resistance and decreases the fuel cell performance.

Increasing the operating temperatures of PEMFCs above 100 °C has significant advantages over conventional room temperature PEM fuel cells and is one of the growing important research areas in fuel cells.[15–20] This includes:[15,16,21] (i) operation at elevated high temperatures substantially enhances the catalytic activity of the electrocatalysts for the O_2 reduction and oxidation reactions of fuels such as hydrogen, methanol and ethanol; (ii) CO tolerance of the catalysts is drastically increased, allowing the use of lower quality reformed hydrogen; (iii) the heat and water management is substantially simplified due to existence of a single water phase and the increased temperature gradient between the fuel cell stack and the coolant and (iv) waste heat can be recovered as a practical energy source. Direct alcohol fuel cells (DAFCs) also benefit significantly from the increased operation temperatures.[6,22,23]

There are extensive research efforts and activities in the development of alternative proton exchange membranes (PEMs) with adequate performance at intermediate temperatures from 100 to 200 °C.[20,24–28] In particular the development of all inorganic material based proton conductors with conductivities greater than 10^{-2} S cm^{-1} in the temperature range of 200–400 °C under low water content is most attractive for the

Fuels and Energy Technology Institute, Department of Chemical Engineering, Curtin University, Perth, WA 6102, Australia. E-mail: s.jiang@curtin.edu.au

high performance direct liquid fuel based fuel cells. A number of biofuels can be directly oxidized or reformed to hydrogen *via* an internal reformer in this temperature range. The operating temperature is also high enough to permit the use of non-precious metal based catalysts with substantially reduced cost for fuel cells. This paper will start with an overview on the progress and achievement of the current high temperature PEMs. And the main focus of the paper will be on the development of nanoporous and mesoporous structured inorganic materials as the new class high temperature PEMs for fuel cells.

2. Overview of the high temperature proton conductor materials

One way to enhance the operation temperature of conventional PEMs is to develop composite membranes with a polymeric matrix and inorganic proton conductive fillers. The inorganic fillers are expected to sequester water and act as a better proton conductor at higher temperature than the pure polymeric membrane. Inorganic metal oxides,[29–33] heteropolyacids,[34–36] mesoporous materials,[33,37,38] zeolites[39,40] and layered, metal phosphates and phosphonates[41] have been used as fillers in composite membranes. Although some of the composite membranes show improved conductivity above 100 °C, they still function better at high RH and also suffer reduced durability due to the additional phase boundaries between the polymeric matrix and inorganic fillers.[42]

Phosphoric acid doped polybenzimidazole (PBI/PA) has been shown to be a promising candidate for a high temperature proton conductive material.[43] With the characterization of self-ionization and self-dehydration, phosphoric acid doped PBI can operate at low relative humidity and elevated high temperatures as compared to Nafion® membranes. Proton conductivities are found to be dependent on the acid doping level, RH and temperature. A conductivity of 6.8×10^{-2} S cm^{-1} is reported for PBI membranes with a PA doping level of 5.6 (H_3PO_4 per repeat unit of PBI) at 200 °C and 5% RH.[43] Xiao *et al.*[44,45] synthesized pyridine-based PBI, using polyphosphoric acid (PPA) as both a solvent and a polycondensation agent, achieving a high proton conductivity of ~0.2 S cm^{-1} at 200 °C. Though PBI/PA PEM fuel cells can run under temperatures from 120 °C to 200 °C, leaching of phosphoric acids during operation is still a significant issue. According to Savadogo and Xing,[46] after working for 125 minutes, the current density of the phosphoric acid–polymer electrolyte decreased to ~60% of the original as a result of the flushing function of the water generated during the fuel cell operation. Another problem is the chemical stability of the polymer matrix. After being exposed at relatively low temperatures of 68 °C for 30 minutes, structural damage appeared in the PBI matrix due to free radicals attack with the existence of H_2O_2 and Fe^{2+}.[47]

Inorganic solid acid composites, such as $CsHSO_4$, CsH_2PO_4 and their derivations have drawn considerable attention due to their superprotonic properties under operating temperatures ranging from 100–300 °C.[25,48] Thermal stability, conductivity at ambient pressure and high pressure of CsH_2PO_4 have been studied by Boysen *et al.*[49] The results show that the phase transition occurs at 228 ± 2 °C and conductivity increases sharply above this temperature. The strong dependence of solid acid compounds on phase transition temperature severely restrict their practical applications in PEMFCs as a result of the difficult start for PEMFCs under low temperatures (<100 °C). The stability of the solid acid in a fuel cell environment is also an issue.[50] To improve the stability of the solid acids, Yamane *et al.*[51] prepared solid solutions of $(CsHSO_4)_{1-x}(CsH_2PO_4)_x$ (x = 0.25–0.75) by a mechanical milling method. The composites were shown to have a superprotonic phase between 20 and 147 °C for $0.25 \leq x \leq 0.75$. However, the stability of these composites depends not only on the composition, but also on the relative humidity.

Different from the oxyanions containing solid acid compounds, metal diphosphate compounds, one of the derivations of phosphoric acid composites, show proton conductivity which is free from the dependence on phase transition.[24] A possible candidate is the ammonium polyphosphate, NH_4PO_3.[52] However, pure ammonium polyphosphate is not stable at temperatures higher than 200 °C. Sun and Stimming[53] studied the proton conductivity properties of the SiO_2–TiO_2–NH_4PO_3 composite prepared by the sol–gel method. The addition of TiO_2 and SiO_2 increased the proton conductivity and the best results were obtained on the composite with 10 mol% TiO_2, 0.043 S cm^{-1} at 225 °C under humidified hydrogen. Hibino *et al.*[54] reported the considerably high proton conductivity of In^{3+}-doped SnP_2O_7 ($Sn_{0.9}In_{0.1}P_2O_7$), 0.1 S cm^{-1} in the temperature range from 150 °C to 350 °C under unhumidified conditions. Huang *et al.*[27,55] studied the proton conductivity properties of niobium and indium doped niobium phosphates. Niobium phosphates show a high proton conductivity of 1.6×10^{-2} S cm^{-1} at 250 °C in dry air and indium doping slightly improves the conductivity. The niobium phosphate based cells show a stable open circuit potential of 0.863 V at 200 °C.[27]

For readers interested in the development and technological challenges of inorganic–organic hybrid materials, PBI/PA composites, metal diphosphate compounds, solid acid compounds and alternative polymeric membranes such as sulfonated PEEK-based polymers as potential high temperature PEMs for fuel cells, various reviews are available.[15,20,24,56–60] In following sections, the emphasis will be on the development and potential application of the inorganic materials with meso- or nanoporous structures as PEMs for fuel cells.

3. Functionalized inorganic mesoporous proton conductors

3.1. TiO_2

Highly ordered mesoporous TiO_2 with uniform pore size (~7.6 nm) and high surface area (271 m^2 g^{-1}) can be synthesized using titanium isopropoxide as a titania source and triblock copolymer P123 as a template.[61] Titanium(IV) oxides of various degrees of hydration, TiO_2,[62–65] $H_2Ti_3O_7$ (ref. 66) and $H_2Ti_4O_9$,[67] have been shown to conduct protons from room temperature to 150 °C. It has been known that the surface of TiO_2 has both

Lewis acid (five-coordinated Ti^{4+} ions) and basic (two-coordinated O^{2-}) sites. Water can be adsorbed on the five-coordinated Ti^{4+} ions in a molecular and/or in a dissociated form.[68] Vichi *et al.*[62,63] investigated the protonic conductivity in a mesoporous TiO_2 membrane as a function of surface chemistry. Changing the surface site density (number of water molecules per square nanometer) from 5.5 to 5.7 leads to an increase in the conductivity from 8.00×10^{-3} to 1.00×10^{-2} S cm^{-1} at 25 °C and 81% RH. The results indicate that values in proton conductivity do not totally correlate with the water content in these materials, indicating that surface chemistry strongly affects the water uptake and proton conductivity of the nanoporous TiO_2. Further studies show that proton conductivity and water uptake of nanoporous TiO_2 is also affected by the pore structure (*e.g.*, porosity, pore size and surface).[69]

Colomer[70] synthesized mesoporous TiO_2 thin films on glass substrates by a sol–gel technique. The films are mesoporous with an average pore diameter of 5.8 nm and the results show that the conductivity improves with the increasing RH, exhibiting a sharp change at ~60% RH (see Fig. 1). The maximum conductivity is 8.71×10^{-3} S cm^{-1} at room temperature and 81% RH and 3.78×10^{-2} S cm^{-1} at 80 °C and 81% RH with an activation energy of 0.23–0.37 eV.[70] Low conductivity in the range of 10^{-4} to 10^{-3} S cm^{-1} measured on pure TiO_2 membranes made by sol–gel methods was also reported by Tsuru *et al.*[71] Titania nanotubes functionalized by 3-mercaptopropyltri-methoxysilane (MPTMS) as the sulfonic acid functional group precursor showed a proton conductivity of 0.08 S cm^{-1} at 80 °C and 100% RH and has been shown to be a good additive to enhance the proton conductivity of Nafion membranes at elevated temperatures and reduced RH.[72]

3.2. Silica and silica based glass

The ordered nanoporous or mesoporous silica materials with high structural order, large surface areas and pore volumes, and easy and variable surface functionalization offer great potential as porous frameworks not only for catalyst supports, protein separation, CO_2 capture[73,74] but also for proton conductors as high temperature PEM applications.[62,70,75–84] Ye *et al.*[85] gave an excellent review on the recent applications of mesoporous materials as electrodes in solar cells, fuel cells and batteries. Due to their high hydrophilicity and capillary condensation effects in the nano-channels they can store and release water at elevated temperatures, facilitating water-assisted proton transport at temperatures above 100 °C. The first reports on ordered mesoporous materials with well-defined pore sizes appeared in 1992 when researchers at Mobil reported for the first time on the synthesis of the M41S family.[86,87] These mesoporous silica, synthesized by the self-assembly method using surfactants as a template, has a large surface area and a uniform pore diameter of several nanometers.[88] The water vapor condenses in pores through capillary force and this occurs at lower water vapor pressures for smaller pores. Thus, a porous structure with a high surface area and small pores is favorable for proton migration. The pore size and pore structure affect the proton conductivity.[75] The proton conductivity has been found to be associated with surface dehydroxylation of porous silica during the heat-treatment. However, high heat-treatment temperature would reduce the hydrophilic nature of the porous silica glass, leading to the reduced conductivity. Li and Kunitake[89] used the oxygen plasma technique to remove the surfactant template, obtaining porous silica thin films at reduced temperatures. The IR data showed that the plasma-treated film had a high retention of the silanol group on the pore wall, as compared to the heat-treated samples. The conductivity of plasma-treated porous silica is 4.8×10^{-4} S cm^{-1} at 90% RH and 50 °C, an order of magnitude higher than that of the heat-treated porous silica under identical conditions.[89] On the other hand, high proton conductivity of 2.0×10^{-2} S cm^{-1} at 80 °C and 81% RH was reported on mesoporous silica xerogels with an average pore size of 3.7 nm.[90] Proton conductivity of mesporous silica and silica xerogels showed a pronounced dependence on RH.[89,90]

Nogami *et al.*[91] studied in detail the proton conductivity in porous silica glass with an average pore size of ~1.7 nm and reported that 0.1 mm thick porous silica glasses sintered at 400 °C exhibited a proton conductivity of $\sim 3 \times 10^{-4}$ S cm^{-1} at 30 °C under high RH. The activation energy for conduction decreases linearly with increasing logarithm of the product of proton and water concentrations, and the conductivity increases with the water concentration, as shown in Fig. 2.[91] Data for glasses containing small amounts of water were from ref. 92. The results indicate that proton conduction in porous silica glasses involves the protons dissociated from SiOH bonds and subsequently migrating or hopping from the initial site to a neighboring site, resulting in the conductivity, as shown below:[91]

$$\mathrm{SiOH}\cdots\mathrm{H_2O} \rightarrow \mathrm{SiO^-} + \mathrm{H^+{:}H_2O} \quad (1)$$

$$\mathrm{H_2O_{(I)}{:}H^+} \rightarrow \mathrm{H_2O_{(I)}} + \mathrm{H^+} \rightarrow \mathrm{H_2O_{(II)}{:}H^+} \quad (2)$$

where the dotted line represents the hydrogen bonding between the proton and the water molecule, $H_2O_{(I)}$ and $H_2O_{(II)}$ are the water molecules that the proton is hopping between. Thus the proton conductivity of porous silica glasses is highly dependent on the water concentration. However, the proton conductivity of pristine mesoporous silica is generally too low (*e.g.*, 10^{-6} S cm^{-1}

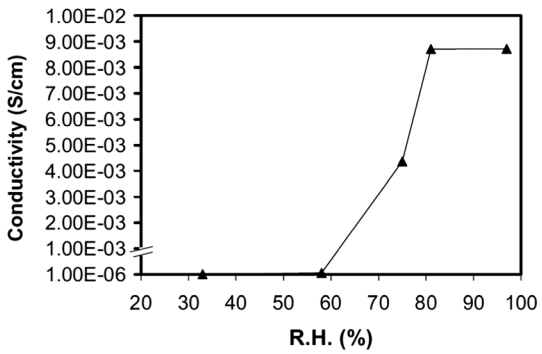

Fig. 1 Proton conductivity of the calcined anatase thin films measured at room temperature under different RH conditions.[70]

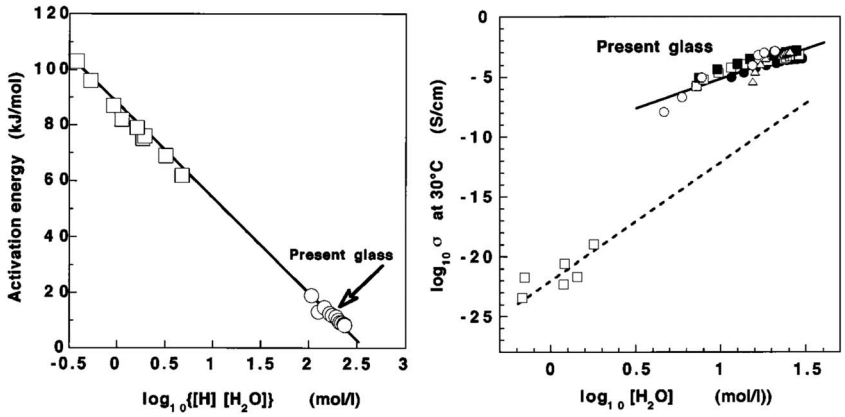

Fig. 2 (a) Relationship between activation energy for conduction and concentration of protons and water, and (b) relationship between the conductivity and logarithm of concentration of water.[91]

to 10^{-4} S cm^{-1} under 40% to 90% RH)[75,93] to be applicable as PEM for fuel cells. Incorporation of aluminium in the mesoporous silica framework can significantly enhance its proton conductivity,[94] as the incorporation of aluminium increases the Brønsted acid sites, enhancing the proton conductivity.

As the protons are generated through the dissociation of adsorbed and condensed water, water dissociation and thus proton conduction can be enhanced by increasing the acidity of the material surface by introducing acid groups, including phosphoric acids,[95,96] sulfonic acids,[84,97] and HNO_3.[63,98] Strong acidity also contributes to retention of water molecules under low water vapor pressure.[63] The acid-functionalized mesoporous silica materials constitute an alternative and promising class of inorganic PEMs for high temperature operations due to their high charge carrier concentration, adjustable acid group density and oxidation resistance. Suzuki *et al.*[99] examined the proton conductivity of phosphorus incorporated mesoporous silica. Incorporation of phosphorus during mesoporous silica formation was found to be effective in improving proton conductivity. A sample with a low P/Si atomic ratio of 0.07 showed the highest proton conductivity above 10^{-2} S cm^{-1} at 100 to 120 °C under saturated water vapor pressure. Nogami *et al*. showed that incorporation of the P=O bond in the glass structure promotes proton dissociation from hydroxyl groups and thus enhances proton conductivity due to the stronger hydrogen bonds.[100] Porous P_2O_5–SiO_2 glass exhibits a significantly high proton conductivity of 2×10^{-2} S cm^{-1} at room temperature and the proton conduction was suggested to be related to the proton hopping between hydroxyl groups and water molecules.[100] Although the phosphate unit improves proton conductivity, it becomes detached from the silicate network upon immersion in water and the conductivity decreases significantly to values similar to those of pure silica.[101] In the case of silicate and phosphate glasses, the content of protons decreases with an increase in the sintering temperature. Thus it is desirable to prepare glasses with a large number of protons at low temperature, like the sol–gel process. The gelation time in the conventional sol–gel process can take as long as 1–6 months.[102] However, the sol–gel process can be accelerated by proper water/vapor management.[103] Increasing the density of the surface group by immersing in protonic acids such as HNO_3 showed marginal improvement in proton conductivity of porous silica.[63,98]

There are many studies focused on the sulfonic acid functionalization.[84,104–108] Ioroi *et al.*[109] prepared nanoporous silica glass with 3-mercaptopropyltrimethoxysilane and subsequent oxidation of the thiol group to sufonic acid groups, achieving a proton conductivity of 1.0×10^{-2} S cm^{-1} at 40 °C and 95% RH. However, operation at high temperatures results in the loss of the grafted HSO_4^- unit. Marschall *et al.* synthesized sulfonic acid functionalized MCM-41 by the microwave assisted co-condensation method.[106] Fig. 3 shows the proton conductivity of SO_3H–MCM-41 synthesized by the microwave assisted co-condensation method.[106] Microwave irradiation has the advantage of oxidation of the thiol group and removal of the template within a short time. Pristine mesoporous silica, MCM-41 shows a negligible conductivity of $\sim 10^{-6}$ S cm^{-1}, which is the result of a partial dissociation of water molecules in the presence of the silanol group. However, SO_3H–MCM-41 composite samples have very high proton conductivity at elevated temperatures, achieving 0.2 S cm^{-1} at 140 °C and 100% RH (Fig. 3a). The proton conductivity of SO_3H–MCM-41 also increases significantly with relative humidity. The proton transfer inside the sulfonic group functionalized mesopores is suggested to be the Grotthus-like mechanism.[106] Nevertheless, no cell performance was presented for the SO_3H–MCM-41 materials. It has been reported that mesoporous silica impregnated with 5.0 M H_2SO_4 shows high conductivities in the order of 10^{-1} S cm^{-1} in a temperature range from 40 to 80 °C at 60% RH.[110] However, the conductivity decreases drastically with time due to a rapid loss of the impregnated H_2SO_4 acid. Marschall *et al.*[111] synthesized imidazole functionalized mesoporous MCM-41 silica by immersing treatment and the highest conductivity was $\sim 10^{-4}$ S cm^{-1} at 140 °C and 100% RH. The proton conductivity of sulfonic acid and imidazole functionalized mesoporous silica composites was found to be very sensitive to RH.[97,111]

Qiao *et al.* studied in detail the proton conductivity properties of phosphoric or phosphonic acid functionalized

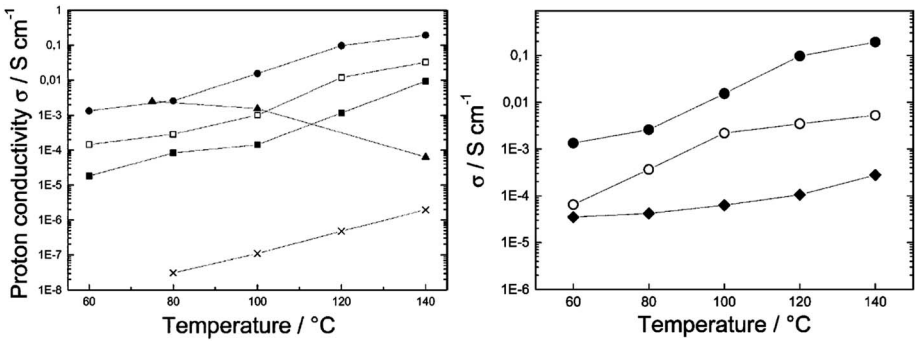

Fig. 3 Proton conductivity measured (a) at 100% RH for 0% (×), 20% (■), 30% (□), and 40% (●) SO_3H–MCM-41 and for Nafion (▲) and (b) on 40% SO_3H–MCM-41 at 0% (◆), 50% (O) and 100% (●) RH.[106]

mesoporous-structured silica as potential membranes for fuel cells.[112,113] Owing to the amphoteric nature of the phosphonic acid, such solids can function as a proton donor (acidic) as well as a proton acceptor (basic) to form dynamic hydrogen bond networks in which protons are transported by breaking and forming of hydrogen bonds. The proton conductivity of phosphonic acid functionalized porous silica nanospheres synthesized by the co-condensation of diethylphosphatoethoxysilane (DPTS) and tetraethoxysilane using the cetyltrimethylammonium bromide surfactant as a template, followed by acidification to phosphoric acid in concentrated HCl, depends strongly on the nominal P/Si ratio, the morphology of the porous silica nanosphere and the RH (Fig. 4).[112] The proton conductivity increases with the humidity and NP40 with most phosphonic acid shows the highest conductivity, 3.0×10^{-4} S cm^{-1} at 20% RH to 0.015 S cm^{-1} at 100% RH at 130 °C. The results indicate that high surface area of the porous silica enhances the proton conductivity under low humidity conditions. However, no stability and cell performance were reported for the phosphoric acid functionalized silica nanosphere composites.

Research has shown that replacing pure silica with a composite silicate of strong acidity, *e.g.*, $Cs_3(H_2PO_4)(HSO_4)_2$–SiO_2,[114] CsH_2SO_4–SiO_2,[115] P_2O_5–SiO_2,[103] P_2O_5–TiO_2–SiO_2 [116] or P_2O_5–ZrO_2–SiO_2 [117] improves the proton conductivity. Due to the higher hydrophilicity of P_2O_5 as compared to SiO_2, the incorporation of P_2O_5 increases the amount of H_2O/OH hydrogen bonding. Tung *et al.*[103] indicated that increasing P_2O_5 content leads to the increased functional groups of P=O and P–OH on the pore surface and reduces the numbers of major pore size channels. The best conductivity is 1.14×10^{-2} S cm^{-1} at 80 °C and 100% RH, obtained on $50P_2O_5$–$50SiO_2$ glass. Nogami *et al.*[118–124] incorporated various heteropolyacids into silicaphosphate porous glass and yielded an electrolyte membrane with proton conductivity of 0.1 S cm^{-1} at 85 °C and 85% RH. The cell based on phosphomolybdic acid (HPMo) incorporated silicaphosphate glass produced a maximum power density of 32 mW cm^{-2} at 29 °C and 30% RH (see Fig. 5).[124] The characteristics of the polarization curves indicate that the cell performance is mainly dominated by the ohmic polarization losses most likely due to the high resistance of the HPMo/ZrO_2–P_2O_5–SiO_2 glass composite membrane.

The power densities reported for silica-based glass PEMs is generally low, from 6 to 41.5 mW cm^{-2} on P_2O_5–SiO_2 and HPW/HPM–P_2O_5–SiO_2 membranes[125,126] to 45 mW cm^{-2} on surface modified silica glass membranes.[109] Using proton conducting H_3PO_4 as a binder, the power density of the P_2O_5–SiO_2 glass membrane cell was 70.3 mW cm^{-2} at 80 °C and 75% RH, which is significantly higher than 28.3 mW cm^{-2} on the same membrane but with PTFE as the binder.[127] Nakamoto *et al.*

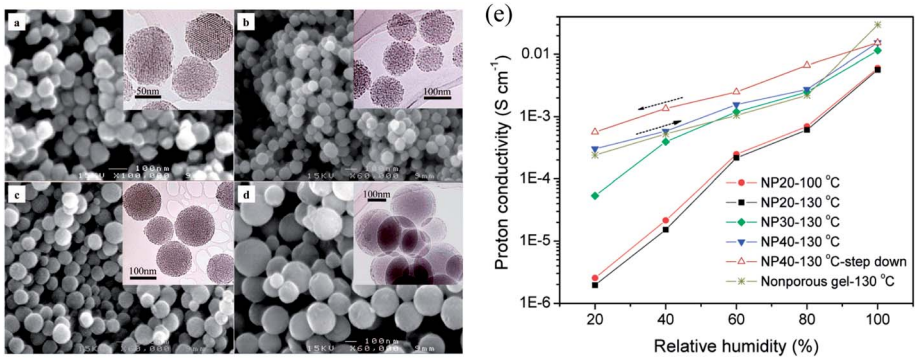

Fig. 4 SEM and TEM (inset) images of (a) NP10, (b) NP20, (c) NP30, and (d) NP40, where NP10, NP20, NP30, and NP40 stands for the nominal P/Si molar ratio of 10%, 20%, 30% and 40% in the acidified product, respectively, and (e) proton conductivity of phosphonic acid functionalized silica nanospheres as a function of RH at 100 and 130 °C.[112]

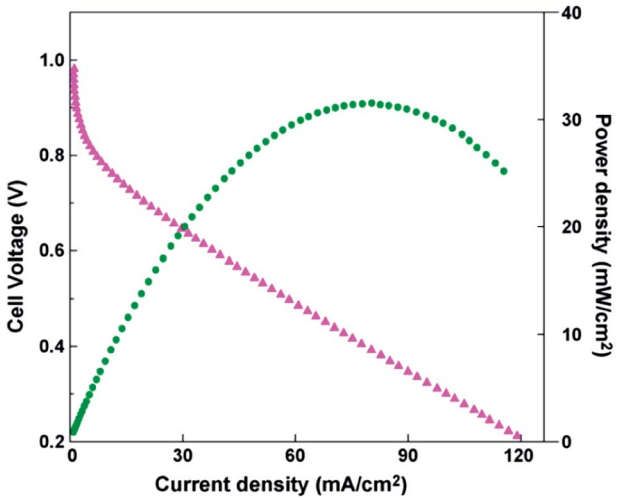

Fig. 5 The H_2/O_2 fuel cell performance of the HPMo/ZrO_2–P_2O_5–SiO_2 (2/4-4-90 mol%) glass composite membrane at 29 °C and 30% RH.[124]

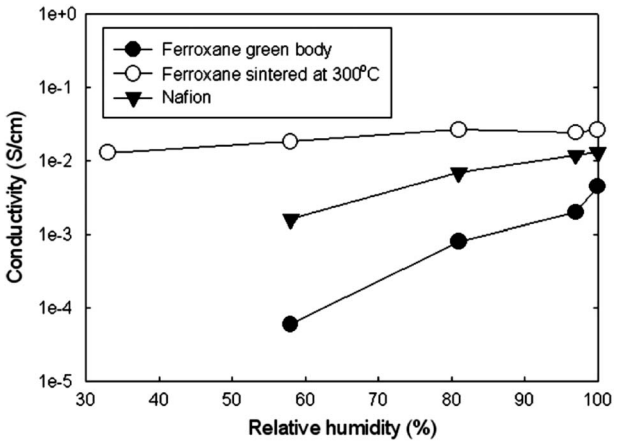

Fig. 6 Plots of proton conductivity of ferroxane green body, ferroxane sintered at 300 °C and Nafion at different humidities. The tests were conducted at room temperature.[138]

obtained maximum power densities of ~25 mW cm^{-2} at 130 °C and 38 mW cm^{-2} at 150 °C using the phosphosilicate gel/polyimide composite membrane.[128] Most recently, Ishiyama *et al.* reported the development of tungsten phosphate glass as PEM for fuel cells.[129] The proton was injected into sodium conductive oxide glass by electrochemical oxidation of hydrogen at the Pd anode and the maximum proton conductivity is 8×10^{-4} S cm^{-1} at 300 °C. The maximum power density of a cell based on the proton injected tungsten phosphate glass membrane is 1.3 mW cm^{-2} at 300 °C. Decreasing the membrane thickness as well as the interface resistance is essential to enhance the cell power output of silica glass based membranes. Di *et al.*[130] introduced a thin Nafion layer to a phosphosilicate glass membrane and the addition of a thin Nafion layer reduced the glass membrane thickness to 500 μm, achieving a peak power density of 207 mW cm^{-2} at 70 °C in H_2/O_2. However, the operation temperature of such MEAs would be limited by the thermal stability of the inserted Nafion layer.

3.3. Al_2O_3 and other ceramic materials

Proton conductivity of porous alumina has also been investigated as the potential application as PEM for fuel cells. Shen *et al.*[131,132] studied the effect of pore size and salt doping on the proton conductivity of mesoporous alumina. Conductivity of mesoporous alumina increased with the pore size and best results were obtained with a pore diameter of 10.8 nm, 4.0×10^{-3} S cm^{-1} at 30 °C and 90% RH. Doping with chloride improves the proton conductivity by 3 to 6 times that of pure alumina. NH_3–TPD analysis showed that chlorine displaces some surface OH and increased the acidity of the mesoporous Al_2O_3, leading to the increase of the proton conductivity.[133] Mesoporous acid-free hematite ceramic membranes have also been studied as proton conductors by Colomer *et al.*[134] This α-Fe_2O_3 ceramic membrane showed a sigmoidal dependence of the conductivity and the water uptake on the RH at a constant temperature. Further study showed that mesoporous α-Fe_2O_3 can also be synthesized from a hydrolytic ferric oxide polymer using a microwave-assisted sol–gel route.[135] Despite the unique acid-free property, the highest conductivity of this α-Fe_2O_3 ceramic membrane is 2.76×10^{-3} S cm^{-1} at 90 °C and 81% RH.[135] Nd_5LnWO_{12} and Ln_6WO_{12} have been found to have satisfactory proton conductivity at high temperature in a hydrogen-containing atmosphere, however, the coexisting electronic conductivity impedes the use in fuel cells.[136]

Tsui *et al.*[137] studied the proton conductivity properties of ceramic membranes derived from ferroxane and alumoxane precursors. The ferroxane derived ceramics, FeOOH fired at 300 °C showed highest proton conductivity from 1.29 to 2.65×10^{-2} S cm^{-1} at relative humidities of 33–100% and room temperature. The conductivity of ferroxane is comparable to that of the Nafion® membrane with the advantages of lower methanol permeability and less sensitivity to humidity, as shown in Fig. 6.[138] However, the ferroxane ceramic membranes are very brittle and can be easily broken to very small pieces. This is mainly due to the poor mechanical properties of the precursor, lepidocrocite as compared to other ceramic materials such as silica and alumina. For example, the hardness of lepidocrocite is 5 GPa, significantly lower than 30.6 GPa obtained on silica.[139] This makes it very hard to fabricate membranes from ferroxane-based ceramic powders.

4. Heteropolyacids functionalized mesoporous silica

In recent years, we concentrated our efforts on the development of heteropolyacids (HPAs)-functionalized mesoporous silica as new inorganic high temperature PEM for fuel cells.[28,140,141] HPAs are known to be a Brønsted acid with unique nano-sized structures and a very strong acidity. Crystallized HPAs contain two types of protons in their structures: the water-combining proton which is dissociated and hydrated, the other is the unhydrated proton located on the bridge-oxygen in the HPAs.[142]

Among HPAs, phosphotungstic acid ($H_3PW_{12}O_{40}$, abbreviated as HPW) has the highest stability and strongest acidity with a high proton conductivity in a fully hydrated state, 0.18 S cm^{-1}.[143] The most common structure is Keggin Unit (KU) as shown in Fig. 7. The central phosphorus (P) atom in a tetrahedral environment is surrounded by 12 octahedra of composition WO_6. The oxygen atoms are shared by tungsten atoms, except for 12 terminal oxygen atoms (O_t) attached to only one addendum atom (W). Normally, protons coordinate to oxygen atoms on the exterior of the KU to construct the primary structure of the HPA. Then adsorbed water molecules interact with oxygen atoms of adjacent KUs *via* hydrogen bonds, linking the units together to form a secondary structure. The effect of water on proton conductivity of HPW is well known, which is pertinent to the use of HPW in the PEM fuel cells.[144–147] Another reason for the selection of HPW as a proton carrier in the *meso*-silica matrix is the high thermal stability, up to 500 °C.[148]

4.1. Synthesis of HPW functionalized mesoporous silica nanocomposites

There are two main approaches to anchor the acid or organic groups onto the inner pore surface of the mesoporous silica: the grafting/impregnation method (post-synthesis) and the co-condensation method (direct or one-pot synthesis). For example, grafting of an organotrialkoxysilane $RSi(OR')_3$ onto the inner surface of the mesoporous silica is well established.[149,150] This method is generic and allows for the incorporation of many different acids and R groups, including bulky ones. The disadvantage of the post-synthesis method is that neither the loading nor the surface distribution of the functional groups as well as their accessibility can be easily controlled. On the other hand, a one-pot synthesis method has the advantages of precise control of the density and distribution of the functional groups along the pores.[106,151,152] Marschall *et al.* showed that the loading of the sulfonic acid group, $-SO_3H$ of the samples synthesized by the co-condensation method is much higher compared to that functionalized by the grafting method.[106,107] Bibent *et al.* synthesized mesoporous SBA-15 with phosphonic, sulfonic and carboxylic acid functional groups by the one-pot synthesis method, see Fig. 8.[153] The acid functionalized mesoporous silica were prepared by co-condensation of the Pluronic 123 (P123, poly(ethylene oxide)–poly(propylene oxide)–poly(ethylene oxide) (PEO–PPO–PEO) block copolymer commercially available as amphiphilic polymers) with a mixture of $[(EtO)_3Si(CH_2)_3–X]$ and tetraethoxysilane (TEOS), where X = $PO(OEt)_2$, SH or CN. The results indicate that the proton conductivity is directly related to the acidity and density of the functional groups anchored to the mesopore surface.

HPW can be incorporated into the mesoporous silica matrix by post-synthesis or by the one-pot self-assembly synthesis process.[28,140] HPW is soluble in water, forming negatively charged $PW_{12}O_{40}^{3-}$ ions. Under normal conditions, the proton adsorption on the SiOH surface groups of the *meso*-silica is very low. However, the presence of HPW decreases the pH of the precursor as HPW is highly acidic in water and this in turn significantly increases the proton adsorption of SiOH groups, forming positively charged $SiOH_2^{+1}$.[154] When HPW molecules, the silica precursor, TEOS are mixed in water, self-assembly occurs between the positively charged silica and the negatively charged HPW by the electrostatic force. With the addition of a

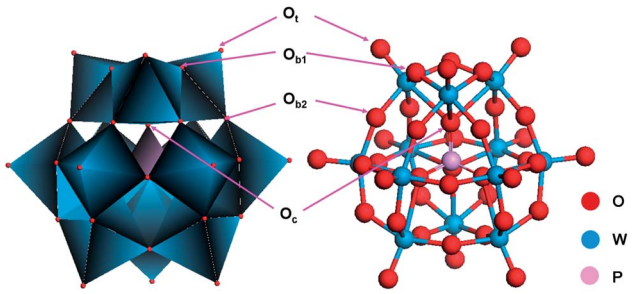

Fig. 7 The Keggin structure of anion phosphotungsitc acid ($PW_{12}O_{40}^{3-}$): O_t, O_{b1}, O_{b2}, and O_c labeled the four types of oxygen in the structure (oxygen atoms in red; tungsten in cyan and phosphor in magenta).

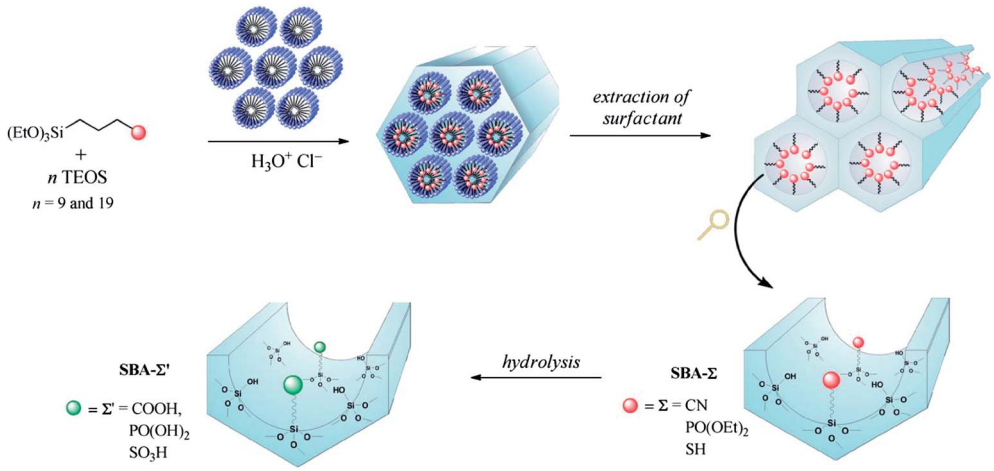

Fig. 8 The synthesis of the acid-functionalized mesoporous silica, SBA–CO_2H, SBA–$PO(OH)_2$ and SBA–SO_3H.[153]

structure-directing agent, P123, the tube-cumulated mesoporous HPW–silica with the template of the P123 surfactant is formed through the cooperative hydrogen bonding and self-assembly between the HPW–silica structure and the P123 surfactant.[88] With the phase separation of P123, the colloidal complex forms ordered mesoporous silica with the HPW self-assembled in the mesoporous structure. The surfactant template is then removed by the heat treatment at 400 °C. In the case of the post-synthesis method, HPW is impregnated into mesopores of mesoporous silica synthesized by methods reported in the literature,[88] followed by solution impregnation preferably under vacuum.[28] Fig. 9 shows the principles of the two synthesis approaches.[148,155]

The HPW loading in the mesoporous silica matrix depends on the synthesis method. In the case of the impregnation route, the HPW loading can be as high as 80 wt%, while the maximum HPW content which can be incorporated into the *meso*-silica structure without any significant detrimental effect on the mesoporous structure is ~25 wt% in the case of the one-pot synthesis route.

4.2. Microstructure, conductivity and performance

4.2.1 Microstructure. The microstructure of HPW functionalized mesoporous silica, HPW–*meso*-silica is related to the synthesis methods. In the case of HPW–*meso*-silica synthesized by a two-step post-synthesis method, the distribution of HPW inside the mesopores can be directly identified by TEM (see Fig. 10).[148] The mesoporous silica host was characterized by highly ordered nano-channels and the channel diameter of mesoporous silica is ~5.2 nm as shown in Fig. 10a. In the case of HPW–*meso*-silica nanocomposites, the distribution of the impregnated HPW nanoparticles in the mesoporous silica matrix is indicated by the ordered but not continuous black

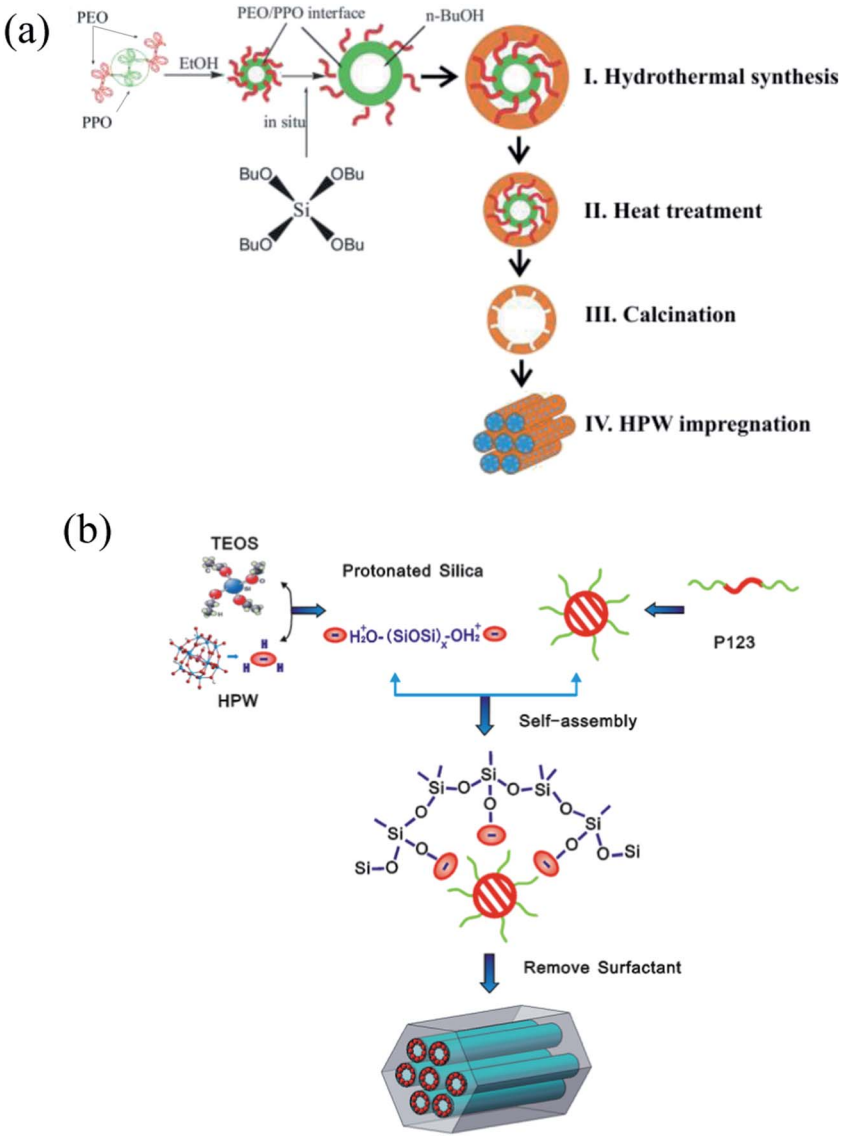

Fig. 9 Schematic of synthesis of HPW–*meso*-silica *via* (a) the two-step HPW impregnation process and (b) the one-step self-assembly process.[148,155]

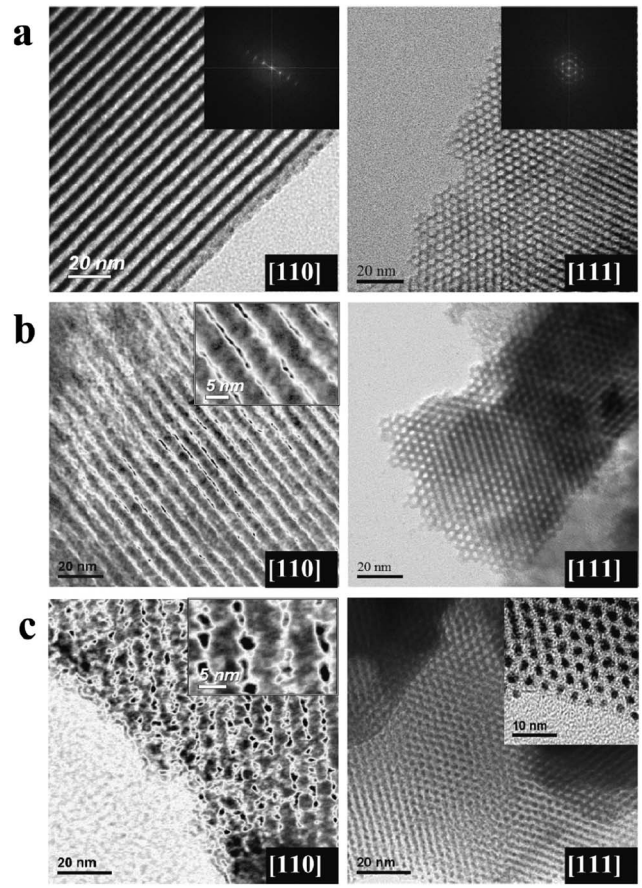

Fig. 10 TEM images of (a) pure *meso*-silica and (b) 20% and (c) 80% HPW–*meso*-silica. The left images were viewed from the [110] direction, whereas the right images were viewed from the [111] direction.[148]

dots sandwiched between continuous channels (grey in color, see Fig. 10b and c). The thick line structure in grey color is siliceous pore walls and the phase contrast between HPW and silica becomes pronounced as the HPW content in the nanocomposite increased to 80 wt% (see the inset, Fig. 10c). Such phase contrast was also observed in the cesium substituted HPA–*meso*-silica system.[156] As the HPW content in *meso*-silica increased to 80 wt%, the density of HPW particles increases, indicating that the distribution of HPW particles in 80% HPW–*meso*-silica is much more uniform than that of 20% HPW–*meso*-silica. The higher intensity of HPW particles inside the *meso*-silica means a shorter pathway of proton transportation, which would lead to the high proton conductivity and low activation energy barriers for the proton conductance in the *meso*-silica matrix. The average distances between the HPW particles in the HPW–*meso*-silica nanocomposites vary between 0 and 5 nm, and the shape and diameter of the interconnected channels of HPW–*meso*-silica nanocomposites are not as regular as that of the pristine *meso*-silica host (the inset, Fig. 10c), probably due to the impregnation and insertion of HPW particles.

The post-synthesis method also has advantages in the flexibility of easy control of mesoporous silica structure symmetries. The pore size and volume can be monitored by variation of the post-synthesis hydrothermal treatment conditions.[157] We investigated recently the HPW–*meso*-silica membrane with mesoporous silica from 2D hexagonal *p6mm*, 3D face-centered cubic ($Fm\bar{3}m$), body-centered $Im\bar{3}m$, to cubic bicontinuous $Ia\bar{3}d$ symmetries.[158] HPW–*meso*-silica nanocomposites with 3D mesostructures display a significantly higher proton conductivity and higher stability as a function of relative humidity in comparison to 2D mesostructures.

The formation and size of micelle and consequently the structure and size of mesopores of mesoporous silica by the one-pot synthesis method are highly dependent on the size of the functional group. This is indicated by the limit of the HPW loading which can be added to the synthesis solution in order to have high density of HPW and at the same time to maintain the high degree of the mesoporous order of the functionalized mesoporous silica.[140,155] Fig. 11 is the TEM micrographs of the ordered mesoporous structure of *meso*-silica with different HPW contents, synthesized *via* the one-pot self-assembly route.[155] The as-synthesized HPW–*meso*-silica structure is characterized by highly ordered 2D nanochannels. The center to center distance of the nanochannels is ~7.3 nm (Fig. 11a). From the TEM images viewing along the pore axis, the diameter of the hexagonal mesostructure is 4.3 nm for 5 wt% HPW–*meso*-silica (Fig. 11b) and 3.8 nm for 25 wt% HPW–*meso*-silica (Fig. 11c). The high-resolution TEM micrograph unambiguously demonstrates that the hexagonal packing of the nanochannels is well-aligned along the zone axis [001] direction. The uniformly ordered mesoporous arrays are still maintained when the HPW content is less than 25 wt%. The top-surface feature is reflective of long-range ordering of the mesochannels and their macroscopic alignment.[159] The results indicate the successful assembly of HPW molecules into the mesoporous SBA-15

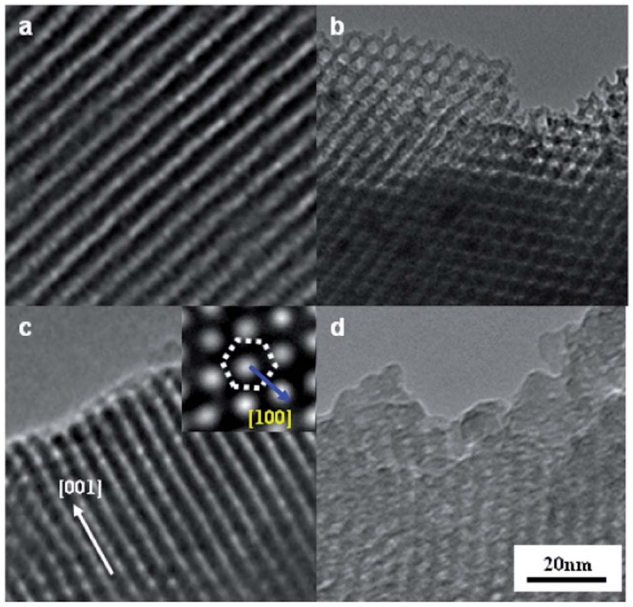

Fig. 11 TEM micrographs of (a) pure SBA-15 silica; (b) 5 wt% HPW–*meso*-silica; (c) 25 wt% HPW–*meso*-silica and (d) 35 wt% HPW–*meso*-silica. The inset in (c) is the TEM image viewing along the pore axis. The scale bar applies to all TEM micrographs.[155]

structure. However, for the 35 wt% self-assembled HPW–*meso*-silica, the mesostructure becomes discontinuous and distorted (see Fig. 11d). The collapse of the ordered mesoporous structure is consistent with the observed significant shrinkage of the diffraction peak (100) of SAXS.[155]

4.2.2 Conductivity and cell performance. Similar to the sulfonic acid functionalized mesoporous silica materials, the proton conductivity of HPW–*meso*-silica nanocomposites depends strongly on the HPW content. In the case of HPW–*meso*-silica nanocomposites *via* the impregnation route, the threshold of HPW content is ~10 wt%. When the HPW content reaches 65–67 wt%, the conductivity is almost independent of the HPW content and has a constant value of 0.07 S cm^{-1} at 25 °C and 100% RH, see Fig. 12.[148] A similar trend was also observed on one-pot self-assembled HPW–*meso*-silica nanocomposites with the maximum conductivity on 25 wt% HPW–*meso*-silica.[155] The proton conductivity is also affected by the structure of the mesoporous silica matrix.[158] The best result was obtained with body-centered cubic ($Im\bar{3}m$)-HPW–*meso*-silica, showing a proton conductivity of 0.061 S cm^{-1} at 25 °C and 0.14 S cm^{-1} at 150 °C under 100% RH, respectively and an activation energy of 10.0 kJ mol^{-1}. Most importantly, the proton conductivity of HPW–*meso*-silica has a much lower sensitivity toward the change in relative humidity. Fig. 13 shows the dependence of the conductivity of a HPW–*meso*-silica nanocomposite on RH measured at 80 °C.[157] In the figure, the proton conductivity of the Nafion 115 membrane was measured at 30 °C as a function of RH. The initial rapid rise in conductivity originates from a change in the hydration state of HPW as the conductivity of HPW is strongly dependent on the number of water molecules contained in the HPW KU (noted as $H_3PW_{12}O_{40}\cdot nH_2O$, $n = 4$–29). However, the RH dependence of the conductivity is far less sensitive as compared to that of Nafion membranes.[160,161] The much less sensitivity of the proton conductivity on the RH indicates the high water retention of the HPW KU-type nanoparticles anchored in the ordered *meso*-silica structure.

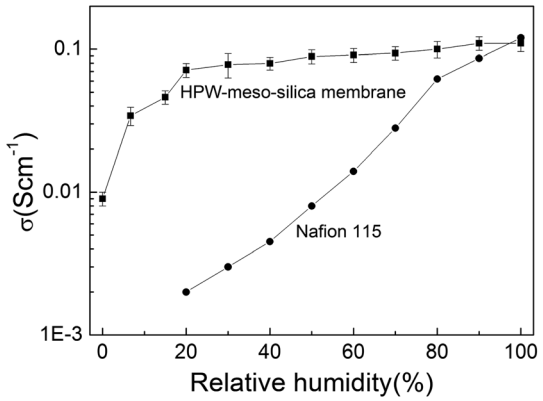

Fig. 13 The conductivity of a HPW–*meso*-silica nanocomposite measured at 80 °C and the reference Nafion 115 membrane measured at 30 °C as a function of relative humidity.[157]

Leaching of acid functional groups from functionalized mesoporous silica is a very important issue for the practical application of the materials as PEMs for fuel cells. The stability of the anchored HPW inside the mesopores was assessed by measuring the stability of proton conductivity of HPW–*meso*-silica under an accelerated durability test with a constant water flow. In the case of a 80% HPW–*meso*-silica, the conductivity value of the nanocomposites drops rather rapidly during the first few hours and reaches a constant value after being tested for 6 h under an accelerated durability test at 80 °C with a constant water flow rate.[28] For example, the conductivity decreased from 0.108 and stabilized at 0.075 S cm^{-1} after the 6 h test and the loss in proton conductivity is 28%.[28] The initial decay in the conductivity is most likely due to the leaching of HPW during the flushing of water. The stability of the impregnated HPW also depends on the pore size. The mesoporous silica with a pore size of ~5 nm shows much higher retention ability for impregnated HPW as compared to that with larger pore size.[157] The stabilized conductivity indicates the successful

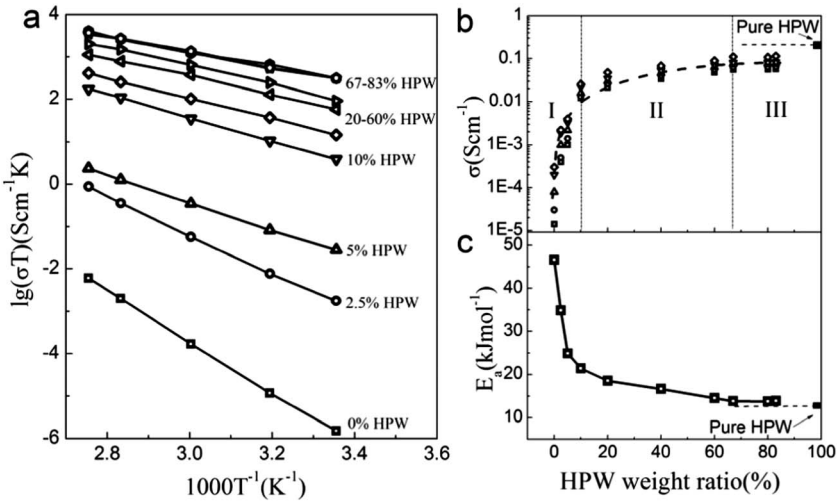

Fig. 12 (a) Proton conductivity *versus* temperature of the HPW–*meso*-silica composite membranes as a function of HPW contents, (b) proton conductivity *versus* HPW content measured at 25 °C, and (c) activation energy *versus* HPW content of HPW–*meso*-silica membrane.[148]

immobilization of water soluble HPW in the mesoporous silica framework. On the other hand, the HPW–*meso*-silica synthesized by the one-pot synthesis method shows very stable proton conductivity under elevated temperatures and reduced RH.[155,162] The stability of HPW inside the mesoporous silica is most likely due to the formation of ($\equiv SiOH_2^+$)($H_2PW_{12}O_{40}^-$) species.[162,163]

The applicability of HPW–*meso*-silica nanocomposite PEMs has been demonstrated in both H_2 and alcohol fuels such as methanol and ethanol on small button cells.[28,155,158,162] Fig. 14 is the typical cell performance for direct methanol and ethanol fuel measured at different temperatures on a cell with a 165 μm-thick 25 wt% HPW–*meso*-silica nanocomposite membrane synthesized *via* the one-pot synthesis method and conventional Pt-based electrocatalysts.[162] The open circuit potential is low, 0.6–0.65 V probably due to the electrolyte membrane which is not 100% dense. The maximum power densities are 16.8 and 43.4 mW cm^{-2} for direct ethanol and methanol at 80 °C, respectively, indicating low electrocatalytic activity of Pt electrocatalysts for the electrochemical oxidation reactions of ethanol and methanol at low temperatures. As the temperature is raised to 200 °C, the maximum power output is 112 mW cm^{-2} for the direct ethanol fuel cell and 128.5 mW cm^{-2} for the direct methanol fuel cell. The DMFC performance based on the HPW–*meso*-silica nanocomposite membrane and low Pt catalyst loading (1 mg cm^{-2}) is close to the advanced DMFCs (100–200 mW cm^{-2}).[164] The preliminary cell stability was tested under a constant current density of 300 mA cm^{-2} at 200 °C for ~1 h. The cell performance indicates the elimination of the poisoning effect of the alcohol oxidation reaction on the Pt black catalysts at elevated high temperatures (Fig. 14b), very different from that commonly observed significant drop in performance for the DAFCs at low temperatures.[165] Further study showed that maximum power density of the cell can be as high as ~240 mW cm^{-2} at 150 °C in 10% RH or under no external humidification in methanol fuel.[155,158] The studies also show that HPW–*meso*-silica nanocomposites have a much lower methanol crossover as compared to the Nafion membranes, most likely due to the gas phase diffusion of methanol and dimensional stability of the inorganic nanocomposite.

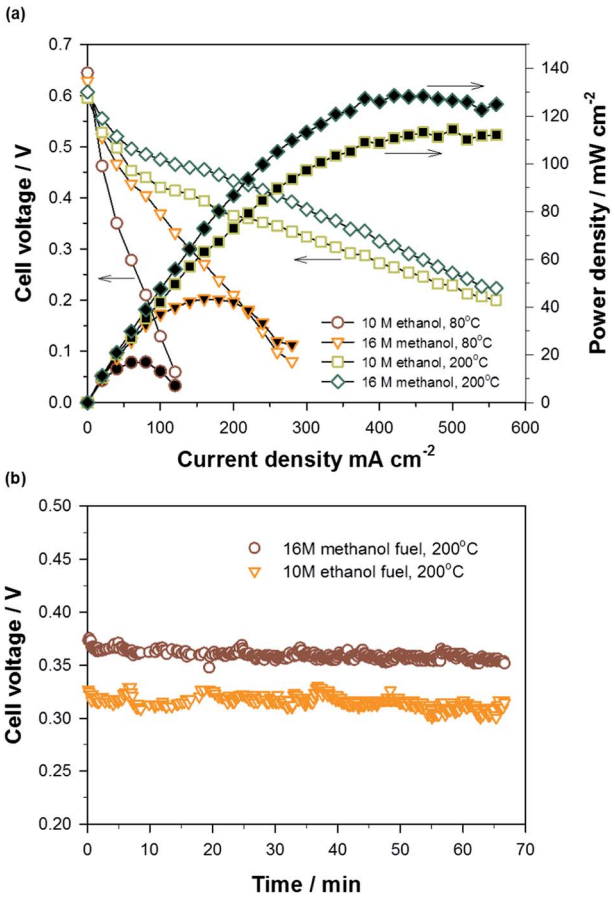

Fig. 14 Performance and stability of single cells assembled by a 165 μm-thick 25 wt% HPW–*meso*-silica nanocomposite membrane for direct alcohol fuel cells in the absence of external humidification. The stability of the cell was measured at a constant current of 300 mA cm^{-2} at 200 °C. Pt black (1.0 mg cm^{-2}) was used as the anode and cathode electrocatalysts.[162]

Demonstration of the performance in stack cells rather than small button cells is an essential step towards the practical application of inorganic PEMs like HPW–*meso*-silica. However, very different from the polymeric membrane such as Nafion and PBI/PA membranes,[166–170] the fabrication of homogeneous, crack-free and mechanically strong membranes with a good working surface area is a significant technological challenge for acid functionalized inorganic materials. Most recently, we successfully fabricated relatively large HPW–*meso*-silica nanocomposite membranes and demonstrated the good performance of the membranes in PEM fuel cell stacks in H_2 without external humidification.[171] HPW–*meso*-silica nanocomposite membranes were fabricated by a modified hot-pressing process so as to increase the mechanical strength and increase the size of membrane. Fig. 15 shows the power output of the 10 cell stack assembled with a 0.76 mm-thick HPW–*meso*-silica membrane and Pt/C as both the catalyst anode and the cathode in H_2/O_2.[171] The OCV of the stack is 7.9 V. The stack produced a maximum power output of 74.4 W, corresponding to a power density of 372.1 mW cm^{-2} at 150 °C in H_2/O_2 based on the total effective cell area of 200 cm^2. This power output is quite high compared to values reported on alternate inorganic membrane fuel cells such as In^{3+} doped SnP_2O_7 (264 mW cm^{-2} at 250 °C),[172] CsH_2PO_4-based electrolyte (48.9 mW cm^{-2} at 235 °C),[173] and HPMo/HPW doped glass electrolytes (32 mW cm^{-2} at 29 °C).[124] The 10 cell stack demonstrates high stability during a 50 h test and generated a near-constant power output of ~32 W in H_2/air (*viz.*, power density of 160 mW cm^{-2}) at 150 °C without external humidification (see Fig. 15b). The results indicate that the HPW–*meso*-silica nanocomposites can be applied in PEM fuel cell stacks operated at elevated temperatures in the absence of external humidification.

4.3. Proton hopping within the HPW–*meso*-silica nanocomposite

Within the HPW–*meso*-silica membrane, the negatively charged heteropolyacids, $PW_{12}O_{40}^{3-}$, are anchored inside the mesoporous silica channels most likely due to the formation of

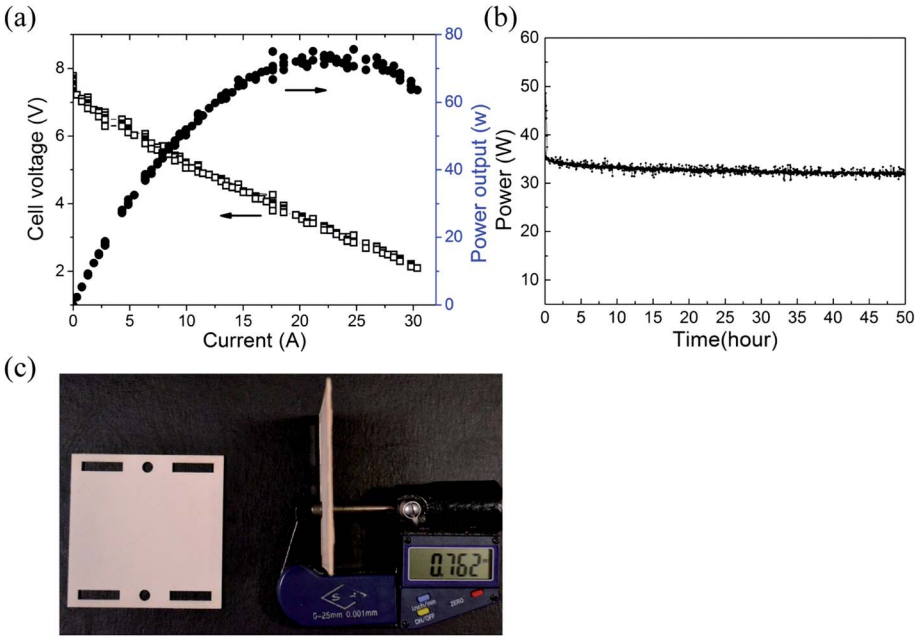

Fig. 15 (a) Polarization and power density of a 10 cell stack measured in H_2/O_2 (1/1 atm) at 150 °C; (b) stability of a 10 cell stack measured at a stack voltage of 6.0 V and 150 °C in H_2/air (1/1 atm). The image in (c) shows a HPW–*meso*-silica membrane with a thickness of 762 μm and a dimension of 62 mm × 62 mm. Note, Pt/C was used as catalyst with a loading of 0.4 mg cm^{-2} for both the anode and the cathode, and the effective area of the stack was 200 cm^2.[171]

($\equiv SiOH_2^+$)($H_2PW_{12}O_{40}^-$) species.[162] As shown in Fig. 10, TEM has provided a direct observation of the morphology and distribution of HPW nanoparticles in the highly ordered mesoporous silica channels, in which the distances between HPW vary according to the weight percentage of HPW. When the content of HPW increases, the average distance between HPWs is accordingly decreased, which leads to the decrease of the energy barrier of proton transfer, so does the increase of the proton conductivity (see Fig. 12).[148,157] For pristine mesoporous silica, the activation energy for proton transfer is 47–55 kJ mol^{-1} and it is 10–14 kJ mol^{-1} for the proton conductivity on HPW–*meso*-silica.[140,148,158] Clearly, the average distances between HPWs, determined by the HPW loading, affect both the proton conductivity and the energy barrier of proton transfer. Fig. 16

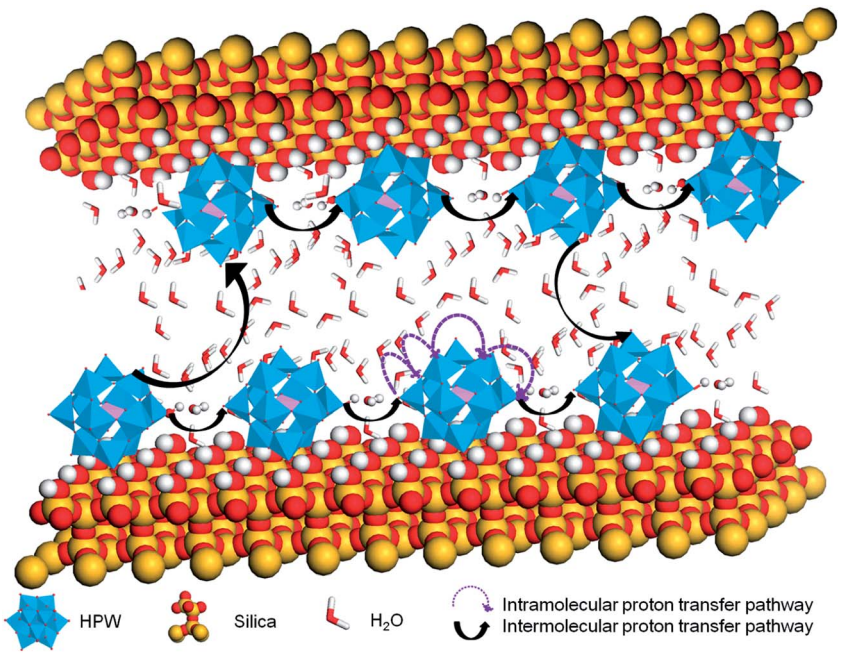

Fig. 16 The proposed proton transportation in HPW–*meso*-silica nanocomposites *via* intramolecular and intermolecular proton hopping.

depicts the effective proton transport pathways in the HPW functionalized mesoporous silica. There are two effective pathways determining the rate of proton transfer. One is the intramolecular proton transfer pathway, in which the proton-hopping happens on an isolated HPW. The other is the intermolecular proton transfer pathway, which differs from the intra-pathway since the proton-exchange process is composed of a series of "hops" from one HPW to the neighboring HPW along the water-assisted hydrogen bond. Obviously, the pathway with higher energy barrier will be the rate-limited step, and determines the overall proton conductivity of the HPW–*meso*-silica nanocomposite.

5. Prospect of functionalized mesoporous silica for high temperature PEMFCs

Table 1 summarizes the properties and performance of typical functionalized mesoporous inorganic material based PEMs. As shown in Table 1, doping of proton conducting agents such as phosphate and sulfuric acids is effective to enhance the proton conductivity of the mesoporous materials. The highest power output was observed on the cell with PA functionalized sintered *meso*-silica membranes, 570 mW cm^{-2} at 190 °C in H_2/O_2.[174,175]

However, for a PEMFC with capability to operate at high temperatures in the range of 200–450 °C it essentially requires a PEM with adequate proton conductivity and stability. To achieve high proton conductivity, the functionalized mesoporous materials must have the capability to retain or hold water under conditions of high temperatures and low RH. As the temperature increases, the total pressure required to maintain the same RH increases dramatically. For example, as shown by Zhang *et al.*[16] to maintain 100% RH at 180 °C requires a total pressure of >10 atm even without considering the partial pressure of fuel and oxidant gas. This essentially places a requirement of the adequate proton conductivity of the functionlized mesoporous materials under very low RH at high temperatures in order to achieve adequate power output under normal operation (*i.e.*, low pressure) conditions. The degree of structural order and size of the mesopores of the porous matrix as well as the structure of the anchored proton carrier have a considerable effect on the water retention properties of the system. On the other hand, the durability of PEMs depends largely on the stability of proton carriers within the mesopores of the matrix, which in turn is related to the nature of the interaction between the dopant and host mesoporous materials. If no chemical bonds are formed between the proton carrier and the exterior surface of the mesoporous matrix, there might be a considerable effect of leaching out the proton carrier due to water produced in a running fuel cell.

Mesoporous materials without doping of the proton carrier generally show significant dependence on the RH. For example, for mesoporous zirconium phosphates, σ is 4.1×10^{-6} at 22 °C and 84% RH and when RH decreases to 30%, σ is $\sim 3.0 \times 10^{-8}$ at the same temperature,[37] resulted in a conductivity decrease by more than two orders of magnitude. Thus, the nature of the proton carrier or conductor is critical. For example, phosphates are lacking chemical stability as P^{5+} ions are easily dissolved in water and become detached from the silicate network.[101] Rapid decrease in conductivity was also observed on the sulfuric acid impregnated mesoporous silica glass membrane due to a partial or total loss of the impregnated acid.[106] Membranes based on phosphate–silicate glasses show the performance at a temperature as high as 300 °C, but the conductivity and cell performance ($\sigma = 8 \times 10^{-4}$ S cm^{-1} and $P = 1.3$ mW cm^{-2} at 300 °C)[129] are probably too low for practical applications. The proton conductivity of phosphate functionalized mesoporous silica also shows high sensitivity to humidity.[112] One of the most fundamental reasons for the leaching of proton carriers such as phosphate and sulfuric acid is most likely the lack of strong chemical bonding between the proton carriers and the ZrO_2, TiO_2 and SiO_2 based mesoporous matrixes.

Mesoporous structures that possess ordered and interconnected networks and high surface areas have shown advantages as the support matrix for the proton carrier when used as PEMs of fuel cells. However, the control of crystallinity, pore size, porosity and ordering in the mesoporous materials is critical to obtain optimum performance as supports for the proton carrier. For example, HPW–*meso*-silica nanocomposites with 3D mesostructures display a significantly higher proton conductivity and higher stability as a function of relative humidity in comparison to 2D mesostructures.[158] For unsupported mesoporous materials, *e.g.*, α-Fe_2O_3 and P_2O_5–SiO_2 glass, high specific surface areas, high pore volume and narrow pore size distribution in the range of 2–3 nm would be required to maintain high water uptake and thus adequate conductivity.[91,127,135] In this case, water molecules within the mesopores play a major role in proton transport by forming protonic charge carriers through hydrogen bonding. On the other hand, size of nano or mesopores is related to the proton carrier or the dopant. In the case of HPW as the proton carrier, pore size in the range of $\sim$6 nm would be sufficient to maintain high proton conductivity and stability.[157] Large pores will lead to a significant loss of the impregnated HPW from the HPW–*meso*-silica nanocomposites. Thermal stability and sintering ability of the mesoporous structure is also an important parameter if the fabrication of the mesoporous materials based membrane involves the high temperature sintering process. For example, the mesoporous structure of TiO_2 is thermally stable at 450 °C,[61] but sintering ability of TiO_2 at this temperature is not known.

As shown here, functionalized mesoporous silica materials show the most promising properties as alternative PEMs for high temperature operation. The proton conductivity of the acid functionalized mesoporous silica is comparable with that of Nafion membranes and under conditions of high temperature and reduced humidity, it is significantly better than Nafion membranes.[84,106,140,148] Among acid functionalized mesoporous silica materials, HPAs such as HPW functionalized mesoporous silica, HPW–*meso*-silica, appears to be most promising, achieving a proton conductivity of 0.14 S cm^{-1} at 150 °C and under anhydrous conditions.[158] The most significant aspect of the HPW–*meso*-silica nanocomposites is the formation of $(\equiv SiOH_2^+)(H_2PW_{12}O_{40}^-)$ species between the positively charged

Table 1 Properties, conductivities and cell performance of functionalized mesoporous materials based PEMFCs

		Properties				
Mesoporous materials	Dopant or functionalization	BET, pore size/nm	Conductivity	Cell performance	Notes	Ref.
Zirconium phosphates	None	177 $m^2 g^{-1}$, 2–4 nm	4.1×10^{-6} S cm^{-1}, 22 °C, 84% RH	n.a.	σ is sensitive to RH.	37
α-Fe_2O_3		239 $m^2 g^{-1}$, 3.8 nm	9.06×10^{-4} S cm^{-1}, 40 °C, 81% RH	n.a.	Highest temp reported: 90 °C	135
FeOOH	None	96 $m^2 g^{-1}$, ~25 nm	0.02 S cm^{-1}, 25 °C, 100% RH	n.a.	Plate-like particles	137
Al_2O_3	None	43.1 $m^2 g^{-1}$, 10.2 nm	4.0×10^{-3} S cm^{-1}, 25 °C, 90% RH	n.a.		131 and 132
Al_2O_3	$LaCl_3$		3.0×10^{-2} S cm^{-1}, 25 °C, 90% RH	n.a.		133
TiO_2	None	134 $m^2 g^{-1}$, ~5 nm	0.01 S cm^{-1}, 25 °C, 81% RH	n.a.	σ is sensitive to RH.	62
TiO_2	Phosphate	134 $m^2 g^{-1}$, ~5 nm	9.7×10^{-3} S cm^{-1}, 25 °C, pH 2.5	n.a.		62
TiO_2 nanotubes	None		5.5×10^{-6} S cm^{-1}, 27 °C, 70% RH	n.a.	Not stable above 150 °C	66
Si–MCM-41	None	1030 $m^2 g^{-1}$, 2.7 nm	1×10^{-6} S cm^{-1}, 140 °C, 100% RH	n.a.		106
5% P_2O_5–95% SiO_2	5% P_2O_5	631 $m^2 g^{-1}$, 2 nm	1.3×10^{-2} S cm^{-1}, 80 °C, 80% RH	70.3 mW cm^{-2} at 80 °C, 75% RH, H_2/O_2	10 wt% H_3PO_4 was used as the binder	127
5%P_2O_5–95% SiO_2	5% P_2O_5	631 $m^2 g^{-1}$, 2 nm	1.0×10^{-3} S cm^{-1}, 80 °C, 80% RH	28.3 mW cm^{-2} at 80 °C, 75% RH, H_2/O_2	10 wt% PTFE was used as the binder	127
ZrO_2–P_2O_5–SiO_2	HPM	~350 $m^2 g^{-1}$, 2.4 nm	10^{-3}–10^{-1} S cm^{-1}, 30–90 °C, 80% RH	32 mW cm^{-2} at 29 °C, 30% RH, H_2/O_2	Active cell area: 0.25 cm^2	124
P_2O_5–SiO_2/ Nafion	None			207 mW cm^{-2} at 70 °C, humidified, H_2/O_2	Nafion layer: 800 nm	130
Si–MCM-41	–SO_3H	1030 $m^2 g^{-1}$, 2.7 nm	0.2 S cm^{-1}, 140 °C, 100% RH	n.a.	σ is sensitive to RH	106
Si–MCM-41	H_3PO_4	~950 $m^2 g^{-1}$, ~2.0 nm	0.015 S cm^{-1}, 130 °C, 100% RH	n.a.	σ is sensitive to RH	112
Si–MCM-41	HPW	~3.0 nm	0.045 S cm^{-1}, 150 °C, 100% RH	95 mW cm^{-2} at 100 °C, 100% RH, H_2/O_2 90 mW cm^{-2} at 150 °C, 1% RH, CH_3OH/O_2	Membrane thickness: 0.8 mm	28
SiO_2	HPW	~950 $m^2 g^{-1}$, 5–8 nm	0.076 S cm^{-1}, 100 °C, 100% RH; 0.05 S cm^{-1}, 200 °C, 0% RH	128.5 mW cm^{-2} at 200 °C, CH_3OH/O_2 112 mW cm^{-2} at 200 °C, CH_3CH_2OH/O_2	Membrane thickness: 0.16 mm; active area: 4 cm^2.	157 and 162
SiO_2	HPW		0.13 S cm^{-1}, 100 °C, 100% RH	74.4 W at 150 °C in H_2/O_2	10 cell stack; membrane thickness: 0.75 mm; active area: 200 cm^2	171
SiO_2, sintered at 650 °C	H_3PO_4	948 $m^2 g^{-1}$, 8.2 nm	0.04 S cm^{-1}, 200 °C, 0% RH	570 mW cm^{-2} at 190 °C, 0% RH, & 700 mW cm^{-2} at 190 °C, 3% RH, H_2/O_2	Membrane thickness: 0.5 mm	174 and 175

siliceous surface of mesoporous silica and negatively charged HPW in the presence of water.[162] This ensures the immobilization and high stability of impregnated or assembled HPW within a highly ordered mesoporous silica structure. The good performance and preliminary stability data of the small button cells and stacks with HPW–*meso*-silica nanocomposite membranes demonstrate that the inorganic PEMs based on highly ordered HPW–*meso*-silica nanocomposites can be applied to the fuel cell operated at temperatures up to 200 °C.

However, silica based materials are inherently inflexible and brittle. Thus it is difficult to fabricate MEAs with good interface contact between the electrode and electrolyte under pressurized conditions similar to that of the polymeric material based membranes. Mechanical strength of the silica based membrane is also a problem and it is very difficult to fabricate MEAs with high density and adequate mechanical strength for handling and operation. Tezuka *et al.* used glass paper as a support for hybrid gel membranes made from 3-glycidoxypropyltrimethoxysilane (GPTMS), tetramethoxysilane (TMOS) and orthophosphoric acid, achieving a power density of 85 mW cm^{-2} at 130 °C and 7% RH.[176] The utilization of glass paper reduces the thickness of the hybrid gel membranes. It is also possible to use

the thin film technique to reduce the thickness of the inorganic material based membranes. Li *et al.* deposited proton conducting thin films of hafnium phosphate and zirconium phosphate/borate/sulfate on smooth ITO glass substrates with thickness of 100–350 nm.[177] However, in practice the quality of the thin film is critically dependent on the morphology and porous structure of the substrates, which also needs to be catalytically active and electronic conducting as electrodes for fuel cells.

As the ceramic materials are generally in the powdered form and thus the membranes fabricated by conventional die pressing techniques need to be in the thickness range of 0.5 to 1.0 mm in order to have sufficient mechanical strength. Nakamoto *et al.* used carbon paper to sandwich phosphosilicate gel and reduced the thickness of the membrane to ~100 μm after hot-press at 130 °C under 11 MPa.[128] However, the use of carbon paper and the polyimide binder limits the thermal stability of the membrane at high temperatures. Thick membranes result in high ohmic losses in the PEMFC. Furthermore, the mechanical strength of the die-pressed discs is still low and brittle in nature, making it very difficult to scale up the system to fuel cell stacks. Very different from the polymeric materials, such difficulty appears to be one of the major obstacles in the development of inorganic material based PEM fuel cells. Another issue is the testing a PEMFC at high temperatures as the temperature increases, the total pressure required to maintain the same RH increases dramatically. This essentially places a requirement of the adequate proton conductivity of the inorganic materials under very low RH at high temperatures in order to utilize the conventional fuel cell test stations. The technical hurdles appear to be indirectly indicated by the observations that majority of the open literature report the excellent proton conductivity of acid functionalized nano or mesoporous ceramic materials such as mesoporous TiO_2, FeOOH, silica or P_2O_5–SiO_2 glass materials but with little or no cell performance.[63,84,91,94,103,106,108,135,153,178,179] Additionally, the use of polymeric binders in the die-pressed discs also limits operation temperatures (200 °C or below) of the PEM due to degradation and decomposition of the polymeric binder.

One of the solutions to substantially increase the operation temperature as well as the mechanical strength is to get rid of the polymeric binder. We have found out recently that mesoporous silica powder can form dense membranes after sintering at 650 °C with the ordered mesoporous structure still intact.[174] The mechanical strength of sintered *meso*-silica is 51 MPa, significantly higher than ~5 MPa on hot-pressed *meso*-silica membranes.[162] The feasibility of utilization of sintered *meso*-silica based PEMs has been demonstrated by functionalization of the sintered *meso*-silica with phosphoric acid (PA) and the results indicate that the PA/sintered *meso*-silica PEM exhibits excellent conductivity under non-humidified conditions, producing a maximum power density of 689 mW cm^{-2} in H_2 at 190 °C in the absence of external humidification.[174]

The mesoporous structure of the sintered *meso*-silica is thermally stable at temperatures up to 650 °C.[175] If HPW instead of PA is used to functionalize sintered mesoporous silica, the HPW/sintered *meso*-silica nanocomposite could be used for PEMFCs operating at temperatures as high as 450 °C, noting that HPW is thermally stable up to 500 °C.[148] Preliminary results indicate the open circuit potential of ~0.85 V and the power output of ~8 mW cm^{-2} at 450 °C in H_2/air using HPW/sintered *meso*-silica nanocomposite PEMs and the Ni anode and the Pt cathode (see Fig. 17). The viability of the operation of PEMFCs in the temperature range of 300–450 °C fills an important temperature gap in current fuel cell technologies and demonstrates the promising potential in the development of new types of fuel cells based on liquid fuels such as methanol and ethanol.

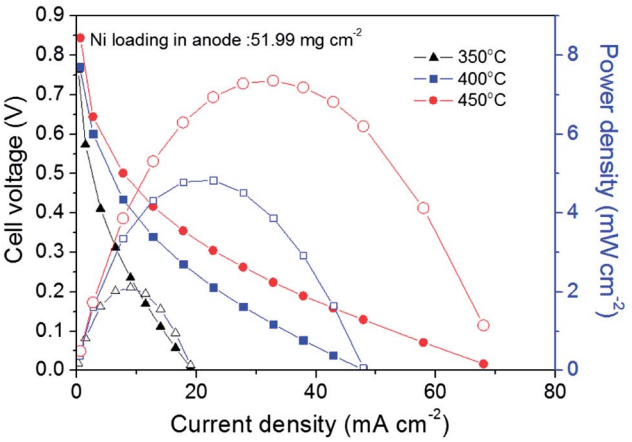

Fig. 17 Power output of a single cell employing a HPW/sintered *meso*-silica nanocomposite membrane using the Ni anode and the Pt cathode in H_2/air at different temperatures (unpublished data).

From a practical point of view, a power output of ~8 mW cm^{-2} would be too low. Thus to substantially increase the cell performance of such functionalized sintered *meso*-silica nanocomposite based PEMFCs, it is necessary to develop and optimize new classes of electrocatalysts for the catalysts/*meso*-silica electrolyte interface. Conventional high surface area carbon-supported Pt based electrocatalysts developed for low temperature fuel cells would not be applicable due to the significant agglomeration of nano-sized Pt catalysts at such high temperatures and oxidation of carbon based supports. However, high operation temperatures in the range of 300–450 °C open a window for the development of non-precious metal and metal oxide based electrocatalysts for fuel cells. Nano-scale and nano-structured electrode concept developed for high temperature solid oxide fuel cells may be applicable for the operation of a PEM fuel cell in the temperatures of 300 to 450 °C.[180] In the meantime, considerably more efforts should be made to fundamentally understand the mesoporous structure–property relationships and mechanism and kinetics of the interfacial reactions and phenomena of fuel cells at temperatures up to 450 °C.

Acknowledgements

This research was supported under the Australian Research Council's *Discovery Projects* funding scheme (project number

DP120102325 & DP120104932). I would like to thank Dr Zhou Yuhua for the assistance in providing the graphics in Fig. 7 and 16.

References

1 P. Costamagna and S. Srinivasan, *J. Power Sources*, 2001, **102**, 242–252.
2 P. Costamagna and S. Srinivasan, *J. Power Sources*, 2001, **102**, 253–269.
3 F. de Bruijn, *Green Chem.*, 2005, **7**, 132–150.
4 S. Gamburzev and A. J. Appleby, *J. Power Sources*, 2002, **107**, 5–12.
5 D. E. Curtin, R. D. Lousenberg, T. J. Henry, P. C. Tangeman and M. E. Tisack, *J. Power Sources*, 2004, **131**, 41–48.
6 A. Brouzgou, A. Podias and P. Tsiakaras, *J. Appl. Electrochem.*, 2013, **43**, 119–136.
7 K. A. Mauritz and R. B. Moore, *Chem. Rev.*, 2004, **104**, 4535–4585.
8 K. D. Kreuer, *J. Membr. Sci.*, 2001, **185**, 29–39.
9 C. Yang, S. Srinivasan, A. B. Bocarsly, S. Tulyani and J. B. Benziger, *J. Membr. Sci.*, 2004, **237**, 145–161.
10 Y. Sone, P. Ekdunge and D. Simonsson, *J. Electrochem. Soc.*, 1996, **143**, 1254–1259.
11 A. V. Anantaraman and C. L. Gardner, *J. Electroanal. Chem.*, 1996, **414**, 115–120.
12 W. H. J. Hogarth, J. C. D. da Costa and G. Q. Lu, *J. Power Sources*, 2005, **142**, 223–237.
13 M. Casciola, G. Alberti, M. Sganappa and R. Narducci, *J. Power Sources*, 2006, **162**, 141–145.
14 Q. F. Li, R. H. He, J. A. Gao, J. O. Jensen and N. J. Bjerrum, *J. Electrochem. Soc.*, 2003, **150**, A1599–A1605.
15 Q. F. Li, R. H. He, J. O. Jensen and N. J. Bjerrum, *Chem. Mater.*, 2003, **15**, 4896–4915.
16 J. L. Zhang, Z. Xie, J. J. Zhang, Y. H. Tanga, C. J. Song, T. Navessin, Z. Q. Shi, D. T. Song, H. J. Wang, D. P. Wilkinson, Z. S. Liu and S. Holdcroft, *J. Power Sources*, 2006, **160**, 872–891.
17 N. L. Garland and J. P. Kopasz, *J. Power Sources*, 2007, **172**, 94–99.
18 M. Doyle, S. K. Choi and G. Proulx, *J. Electrochem. Soc.*, 2000, **147**, 34–37.
19 H. W. Zhang and P. K. Shen, *Chem. Soc. Rev.*, 2012, **41**, 2382–2394.
20 A. Iulianelli and A. Basile, *Int. J. Hydrogen Energy*, 2012, **37**, 15241–15255.
21 C. Yang, P. Costamagna, S. Srinivasan, J. Benziger and A. B. Bocarsly, *J. Power Sources*, 2001, **103**, 1–9.
22 H. Ahmad, S. K. Kamarudin, U. A. Hasran and W. R. W. Daud, *Int. J. Hydrogen Energy*, 2010, **35**, 2160–2175.
23 V. Neburchilov, J. Martin, H. J. Wang and J. J. Zhang, *J. Power Sources*, 2007, **169**, 221–238.
24 O. Paschos, J. Kunze, U. Stimming and F. Maglia, *J. Phys.: Condens. Matter*, 2011, **23**, 234110.
25 S. M. Haile, D. A. Boysen, C. R. I. Chisholm and R. B. Merle, *Nature*, 2001, **410**, 910–913.
26 P. Heo, M. Nagao, M. Sano and T. Hibino, *J. Electrochem. Soc.*, 2008, **155**, B92–B95.
27 Y. Huang, Q. F. Li, A. H. Jensen, M. Yin, J. O. Jensen, E. Christensen, C. Pan, N. J. Bjerrum and W. Xing, *J. Mater. Chem.*, 2012, **22**, 22452–22458.
28 S. F. Lu, D. L. Wang, S. P. Jiang, Y. Xiang, J. L. Lu and J. Zeng, *Adv. Mater.*, 2010, **22**, 971–976.
29 K. T. Adjemian, S. J. Lee, S. Srinivasan, J. Benziger and A. B. Bocarsly, *J. Electrochem. Soc.*, 2002, **149**, A256–A261.
30 R. Zeng, Y. Wang, S. L. Wang and P. K. Shen, *Electrochim. Acta*, 2007, **52**, 3895–3900.
31 B. P. Ladewig, R. B. Knott, A. J. Hill, J. D. Riches, J. W. White, D. J. Martin, J. C. D. da Costa and G. Q. Lu, *Chem. Mater.*, 2007, **19**, 2372–2381.
32 S. P. Nunes, B. Ruffmann, E. Rikowski, S. Vetter and K. Richau, *J. Membr. Sci.*, 2002, **203**, 215–225.
33 F. Pereira, K. Valle, P. Belleville, A. Morin, S. Lambert and C. Sanchez, *Chem. Mater.*, 2008, **20**, 1710–1718.
34 Y. S. Kim, F. Wang, M. Hickner, T. A. Zawodzinski and J. E. McGrath, *J. Membr. Sci.*, 2003, **212**, 263–282.
35 B. Tazi and O. Savadogo, *Electrochim. Acta*, 2000, **45**, 4329–4339.
36 L. Wang, B. L. Yi, H. M. Zhang and D. M. Xing, *Electrochim. Acta*, 2007, **52**, 5479–5483.
37 W. H. J. Hogarth, J. C. D. da Costa, J. Drennan and G. Q. Lu, *J. Mater. Chem.*, 2005, **15**, 754–758.
38 J. H. Won, H. J. Lee, K. S. Yoon, Y. T. Hong and S. Y. Lee, *Int. J. Hydrogen Energy*, 2012, **37**, 9202–9211.
39 V. Baglio, A. S. Arico, A. Di Blasi, P. L. Antonucci, F. Nannetti, V. Tricoli and V. Antonucci, *J. Appl. Electrochem.*, 2005, **35**, 207–212.
40 X. Li, E. P. L. Roberts, S. M. Holmes and V. Zholobenko, *Solid State Ionics*, 2007, **178**, 1248–1255.
41 G. Alberti and M. Casciola, *Annu. Rev. Mater. Res.*, 2003, **33**, 129–154.
42 H. Tang, Z. Wan, M. Pan and S. P. Jiang, *Electrochem. Commun.*, 2007, **9**, 2003–2008.
43 R. H. He, Q. F. Li, G. Xiao and N. J. Bjerrum, *J. Membr. Sci.*, 2003, **226**, 169–184.
44 L. Xiao, H. Zhang, T. Jana, E. Scanlon, R. Chen, E. W. Choe, L. S. Ramanathan, S. Yu and B. C. Benicewicz, *Fuel Cells*, 2005, **5**, 287–295.
45 L. X. Xiao, H. F. Zhang, E. Scanlon, L. S. Ramanathan, E. W. Choe, D. Rogers, T. Apple and B. C. Benicewicz, *Chem. Mater.*, 2005, **17**, 5328–5333.
46 O. Savadogo and B. Xing, *J. New Mater. Electrochem. Syst.*, 2000, **3**, 343–347.
47 Q. Li, C. Pan, J. O. Jensen, P. Noye and N. J. Bjerrum, *Chem. Mater.*, 2007, **19**, 350–352.
48 W. Zhou, A. S. Bondarenko, B. A. Boukamp and H. J. M. Bouwmeester, *Solid State Ionics*, 2008, **179**, 380–384.
49 D. A. Boysen, S. M. Haile, H. J. Liu and R. A. Secco, *Chem. Mater.*, 2003, **15**, 727–736.
50 R. B. Merle, C. R. I. Chisholm, D. A. Boysen and S. M. Haile, *Energy Fuels*, 2003, **17**, 210–215.
51 Y. Yamane, K. Yamada and K. Inoue, *Solid State Ionics*, 2008, **179**, 483–488.

52 M. Cappadonia, O. Niemzig and U. Stimming, *Solid State Ionics*, 1999, **125**, 333–337.
53 C. Sun and U. Stimming, *Electrochim. Acta*, 2008, **53**, 6417–6422.
54 P. Heo, H. Shibata, M. Nagao and T. Hibino, *Solid State Ionics*, 2008, **179**, 1446–1449.
55 Y. J. Huang, Q. F. Li, T. V. Anfimova, E. Christensen, M. Yin, J. O. Jensen, N. J. Bjerrum and W. Xing, *Int. J. Hydrogen Energy*, 2013, **38**, 2464–2470.
56 A. Goni-Urtiaga, D. Presvytes and K. Scott, *Int. J. Hydrogen Energy*, 2012, **37**, 3358–3372.
57 S. J. Peighambardoust, S. Rowshanzamir and M. Amjadi, *Int. J. Hydrogen Energy*, 2010, **35**, 9349–9384.
58 S. Bose, T. Kuila, X. L. N. Thi, N. H. Kim, K. T. Lau and J. H. Lee, *Prog. Polym. Sci.*, 2011, **36**, 813–843.
59 J. A. Asensio, E. M. Sanchez and P. Gomez-Romero, *Chem. Soc. Rev.*, 2010, **39**, 3210–3239.
60 L. Wu, Z. H. Zhang, J. Ran, D. Zhou, C. R. Li and T. W. Xu, *Phys. Chem. Chem. Phys.*, 2013, **15**, 4870–4887.
61 W. Y. Dong, Y. J. Sun, C. W. Lee, W. M. Hua, X. C. Lu, Y. F. Shi, S. C. Zhang, J. M. Chen and D. Y. Zhao, *J. Am. Chem. Soc.*, 2007, **129**, 13894–13904.
62 F. M. Vichi, M. I. Tejedor-Tejedor and M. A. Anderson, *Chem. Mater.*, 2000, **12**, 1762–1770.
63 F. M. Vichi, M. T. Colomer and M. A. Anderson, *Electrochem. Solid-State Lett.*, 1999, **2**, 313–316.
64 T. Kasuga, *Thin Solid Films*, 2006, **496**, 141–145.
65 H. Ekstrom, B. Wickman, M. Gustavsson, P. Hanarp, L. Eurenius, E. Olsson and G. Lindbergh, *Electrochim. Acta*, 2007, **52**, 4239–4245.
66 A. Thorne, A. Kruth, D. Tunstall, J. T. S. Irvine and W. Z. Zhou, *J. Phys. Chem. B*, 2005, **109**, 5439–5444.
67 E. K. Andersen, J. G. K. Andersen and E. Skou, *Solid State Ionics*, 1988, **27**, 181–187.
68 T. Bredow and K. Jug, *Surf. Sci.*, 1995, **327**, 398–408.
69 M. I. Tejedor-Tejedor, F. M. Vichi and M. A. Anderson, *J. Porous Mater.*, 2005, **12**, 201–214.
70 M. T. Colomer, *Adv. Mater.*, 2006, **18**, 371–374.
71 T. Tsuru, Y. Yagi, Y. Kinoshita and M. Asada, *Solid State Ionics*, 2003, **158**, 343–350.
72 Y. Jun, H. Zarrin, M. Fowler and Z. W. Chen, *Int. J. Hydrogen Energy*, 2011, **36**, 6073–6081.
73 A. Kaithwas, M. Prasad, A. Kulshreshtha and S. Verma, *Chem. Eng. Res. Des.*, 2012, **90**, 1632–1641.
74 J. J. Zhu, T. Wang, X. L. Xu, P. Xiao and J. L. Li, *Appl. Catal., B*, 2013, **130**, 197–217.
75 H. B. Li and M. Nogami, *Adv. Mater.*, 2002, **14**, 912–914.
76 G. L. Athens, Y. Ein-Eli and B. F. Chmelka, *Adv. Mater.*, 2007, **19**, 2580–2583.
77 M. Yamada, D. L. Li, I. Honma and H. S. Zhou, *J. Am. Chem. Soc.*, 2005, **127**, 13092–13093.
78 Y. Daiko, T. Kasuga and M. Nogami, *Chem. Mater.*, 2002, **14**, 4624–4627.
79 H. B. Li and M. Nogami, *Chem. Commun.*, 2003, 236–237.
80 T. Uma and M. Nogami, *Chem. Mater.*, 2007, **19**, 3604–3610.
81 L. M. Xiong and M. Nogami, *Chem. Lett.*, 2006, **35**, 972–973.
82 J. D. Halla, M. Mamak, D. E. Williams and G. A. Ozin, *Adv. Funct. Mater.*, 2003, **13**, 133–138.
83 S. N. Azizi, S. Ghasemi and E. Chiani, *Electrochim. Acta*, 2013, **88**, 463–472.
84 B. Y. Jiang, H. L. Tang and M. Pan, *Int. J. Hydrogen Energy*, 2012, **37**, 4612–4618.
85 Y. Ye, C. Jo, I. Jeong and J. Lee, *Nanoscale*, 2013, **5**, 4584–4605.
86 J. S. Beck, J. C. Vartuli, W. J. Roth, M. E. Leonowicz, C. T. Kresge, K. D. Schmitt, C. T. W. Chu, D. H. Olson, E. W. Sheppard, S. B. McCullen, J. B. Higgins and J. L. Schlenker, *J. Am. Chem. Soc.*, 1992, **114**, 10834–10843.
87 C. T. Kresge, M. E. Leonowicz, W. J. Roth, J. C. Vartuli and J. S. Beck, *Nature*, 1992, **359**, 710–712.
88 Y. Wan and D. Y. Zhao, *Chem. Rev.*, 2007, **107**, 2821–2860.
89 H. B. Li and T. Kunitake, *Microporous Mesoporous Mater.*, 2006, **97**, 42–48.
90 M. T. Colomer, F. Rubio and J. R. Jurado, *J. Power Sources*, 2007, **167**, 53–57.
91 M. Nogami, R. Nagao and C. Wong, *J. Phys. Chem. B*, 1998, **102**, 5772–5775.
92 M. Nogami and Y. Abe, *Phys. Rev. B: Condens. Matter Mater. Phys.*, 1997, **55**, 12108–12112.
93 Y. Daiko, T. Kasuga and M. Nogami, *Microporous Mesoporous Mater.*, 2004, **69**, 149–155.
94 M. Sharifi, R. Marschall, M. Wilkening and M. Wark, *J. Power Sources*, 2010, **195**, 7781–7786.
95 M. Nogami, H. B. Li, Y. Daiko and T. Mitsuoka, *J. Sol-Gel Sci. Technol.*, 2004, **32**, 185–188.
96 H. B. Li, D. L. Jin, X. Y. Kong, H. Y. Tu, Q. C. Yu and F. J. Jiang, *Microporous Mesoporous Mater.*, 2011, **138**, 63–67.
97 R. Marschall, I. Bannat, A. Feldhoff, L. Z. Wang, G. Q. Lu and M. Wark, *Small*, 2009, **5**, 854–859.
98 M. T. Colomer and M. A. Anderson, *J. Non-Cryst. Solids*, 2001, **290**, 93–104.
99 S. Suzuki, Y. Nozaki, T. Okumura and M. Miyayama, *J. Ceram. Soc. Jpn.*, 2006, **114**, 303–307.
100 M. Nogami, R. Nagao, G. Wong, T. Kasuga and T. Hayakawa, *J. Phys. Chem. B*, 1999, **103**, 9468–9472.
101 M. Nogami, Y. Goto, Y. Tsurita and T. Kasuga, *J. Am. Ceram. Soc.*, 2001, **84**, 2553–2556.
102 C. Wang and M. Nogami, *Mater. Lett.*, 2000, **42**, 225–228.
103 S. P. Tung and B. J. Hwang, *J. Mater. Chem.*, 2005, **15**, 3532–3538.
104 S. Mikhailenko, D. Desplantier-Giscard, C. Danumah and S. Kaliaguine, *Microporous Mesoporous Mater.*, 2002, **52**, 29–37.
105 D. Margolese, J. A. Melero, S. C. Christiansen, B. F. Chmelka and G. D. Stucky, *Chem. Mater.*, 2000, **12**, 2448–2459.
106 R. Marschall, J. Rathousky and M. Wark, *Chem. Mater.*, 2007, **19**, 6401–6407.
107 R. Marschall, I. Bannat, J. Caro and M. Wark, *Microporous Mesoporous Mater.*, 2007, **99**, 190–196.
108 R. Supplit, A. Sugawara, H. Peterlik, R. Kikuchi and T. Okubo, *Eur. J. Inorg. Chem.*, 2010, 3993–3999.

109 T. Ioroi, K. Kuraoka, K. Yasuda, T. Yazawa and Y. Miyazaki, *Electrochem. Solid-State Lett.*, 2004, **7**, A394–A396.
110 A. Matsuda, T. Kanzaki, K. Tadanaga, T. Kogure, M. Tatsumisago and T. Minami, *J. Electrochem. Soc.*, 2002, **149**, E292–E297.
111 R. Marschall, M. Sharifi and M. Wark, *Microporous Mesoporous Mater.*, 2009, **123**, 21–29.
112 Y. G. Jin, S. Z. Qiao, Z. P. Xu, J. C. D. da Costa and G. Q. Lu, *J. Phys. Chem. C*, 2009, **113**, 3157–3163.
113 Y. G. Jin, S. Z. Qiao, Z. P. Xu, Z. M. Yan, Y. N. Huang, J. C. D. da Costa and G. Q. Lu, *J. Mater. Chem.*, 2009, **19**, 2363–2372.
114 V. G. Ponomareva and E. S. Shutova, *Solid State Ionics*, 2005, **176**, 2905–2908.
115 V. G. Ponomareva and E. S. Shutova, *Solid State Ionics*, 2007, **178**, 729–734.
116 M. Nogami, R. Nagao, C. Wong, T. Kasuga and T. Hayakawa, *J. Phys. Chem. B*, 1999, **103**, 9468–9472.
117 M. Nogami, Y. Daiko, T. Akai and T. Kasuga, *J. Phys. Chem. B*, 2001, **105**, 4653–4656.
118 T. Uma and M. Nogami, *J. Membr. Sci.*, 2008, **323**, 11–16.
119 T. Uma and M. Nogami, *Anal. Chem.*, 2008, **80**, 506–508.
120 T. Inoue, T. Uma and M. Nogami, *J. Membr. Sci.*, 2008, **323**, 148–152.
121 T. Uma and M. Nogami, *Fuel Cells*, 2007, **7**, 279–284.
122 T. Uma and M. Nogami, *Chem. Mater.*, 2007, **19**, 3604–3610.
123 T. Uma and M. Nogami, *J. Electrochem. Soc.*, 2007, **154**, B845–B851.
124 T. Uma and M. Nogami, *J. Membr. Sci.*, 2009, **334**, 123–128.
125 M. Nogami, H. Matsushita, Y. Goto and T. Kasuga, *Adv. Mater.*, 2000, **12**, 1370–1372.
126 T. Uma and M. Nogami, *Anal. Chem.*, 2008, **80**, 506–508.
127 M. Nogami, K. Tanaka and T. Uma, *Fuel Cells*, 2009, **9**, 528–533.
128 N. Nakamoto, A. Matsuda, K. Tadanaga, T. Minami and M. Tatsumisago, *J. Power Sources*, 2004, **138**, 51–55.
129 T. Ishiyama, S. Suzuki, J. Nishii, T. Yamashita, H. Kawazoe and T. Omata, *J. Electrochem. Soc.*, 2013, **160**, E143–E147.
130 Z. G. Di, H. B. Li, M. Li, D. L. Mao, X. J. Chen, M. Xiao and J. Gu, *J. Power Sources*, 2012, **207**, 86–90.
131 H. Shen, H. Maekawa, J. Kawamura, Y. Matsumoto, T. Yamamura, Y. Kawakita, K. Shibata and M. Kawai, *Solid State Ionics*, 2008, **179**, 1133–1137.
132 H. Y. Shen, H. Maekawa, J. Kawamura and T. Yamamura, *Solid State Ionics*, 2006, **177**, 2403–2406.
133 H. Shen, H. Maekawa, L. Wang, B. Guo and K. Y. Shu, *Electrochem. Solid-State Lett.*, 2009, **12**, B18–B21.
134 M. T. Colomer, *J. Power Sources*, 2011, **196**, 8280–8285.
135 M. T. Colomer and K. Zenzinger, *Microporous Mesoporous Mater.*, 2012, **161**, 123–133.
136 S. Escolastico, C. Solis and J. M. Serra, *Int. J. Hydrogen Energy*, 2011, **36**, 11946–11954.
137 E. M. Tsui, M. M. Cortalezzi and M. R. Wiesner, *J. Membr. Sci.*, 2007, **306**, 8–15.
138 L. W. Zhang, S. R. Chae, Z. Hendren, J. S. Park and M. R. Wiesner, *Chem. Eng. J.*, 2012, **204**, 87–97.
139 F. M. Gao, J. L. He, E. D. Wu, S. M. Liu, D. L. Yu, D. C. Li, S. Y. Zhang and Y. J. Tian, *Phys. Rev. Lett.*, 2003, **91**, 015502.
140 H. L. Tang, M. Pan, S. F. Lu, J. L. Lu and S. P. Jiang, *Chem. Commun.*, 2010, **46**, 4351–4353.
141 S. P. Jiang, *Solid State Ionics*, 2013, in press.
142 M. Amirinejad, S. S. Madaeni, E. Rafiee and S. Amirinejad, *J. Membr. Sci.*, 2011, **377**, 89–98.
143 O. Nakamura, T. Kodama, I. Ogino and Y. Miyake, *Chem. Lett.*, 1979, 17–18.
144 D. L. Wang, S. F. Lu and S. P. Jiang, *Chem. Commun.*, 2010, **46**, 2058–2060.
145 Y. Xiang, M. Yang, J. Zhang, F. Lan and S. F. Lu, *J. Membr. Sci.*, 2011, **368**, 241–245.
146 T. Kukino, R. Kikuchi, T. Takeguchi, T. Matsui and K. Eguchi, *Solid State Ionics*, 2005, **176**, 1845–1848.
147 Z. M. Cui, W. Xing, C. P. Liu, D. Tian and H. Zhang, *J. Power Sources*, 2010, **195**, 1619–1623.
148 J. Zeng and S. P. Jiang, *J. Phys. Chem. C*, 2011, **115**, 11854–11863.
149 L. Mercier and T. J. Pinnavaia, *Adv. Mater.*, 1997, **9**, 500–503.
150 A. Cauvel, G. Renard and D. Brunel, *J. Org. Chem.*, 1997, **62**, 749–751.
151 R. J. P. Corriu, C. Hoarau, A. Mehdi and C. Reye, *Chem. Commun.*, 2000, 71–72.
152 D. J. Macquarrie, *Chem. Commun.*, 1996, 1961–1962.
153 N. Bibent, A. Mehdi, G. Silly, F. Henn and S. Devautour-Vinot, *Eur. J. Inorg. Chem.*, 2011, 3214–3225.
154 A. Pettersson and J. B. Rosenholm, *Langmuir*, 2002, **18**, 8447–8454.
155 J. L. Lu, H. L. Tang, S. F. Lu, H. W. Wu and S. P. Jiang, *J. Mater. Chem.*, 2011, **21**, 6668–6676.
156 P. M. Rao, P. Goldberg-Oppenheimer, S. Kababya, S. Vega and M. Landau, *J. Mol. Catal. A: Chem.*, 2007, **275**, 214–227.
157 J. Zeng, Y. H. Zhou, L. Li and S. P. Jiang, *Phys. Chem. Chem. Phys.*, 2011, **13**, 10249–10257.
158 J. Zeng, P. K. Shen, S. F. Lu, Y. Xiang, L. Li, R. De Marco and S. P. Jiang, *J. Membr. Sci.*, 2012, **397**, 92–101.
159 R. Fan, S. Huh, R. Yan, J. Arnold and P. D. Yang, *Nat. Mater.*, 2008, **7**, 303–307.
160 Y. S. Ye, W. Y. Chen, Y. J. Huang, M. Y. Cheng, Y. C. Yen, C. C. Cheng and F. C. Chang, *J. Membr. Sci.*, 2010, **362**, 29–37.
161 X. M. Yan, P. Mei, Y. Z. Mi, L. Gao and S. X. Qin, *Electrochem. Commun.*, 2009, **11**, 71–74.
162 H. L. Tang, M. Pan and S. P. Jiang, *Dalton Trans.*, 2011, **40**, 5220–5227.
163 F. Lefebvre, *J. Chem. Soc., Chem. Commun.*, 1992, 756–757.
164 S. C. Thomas, X. M. Ren, S. Gottesfeld and P. Zelenay, *Electrochim. Acta*, 2002, **47**, 3741–3748.
165 S. Wasmus and A. Kuver, *J. Electroanal. Chem.*, 1999, **461**, 14–31.
166 E. A. Cho, U. S. Jeon, S. A. Hong, I. H. Oh and S. G. Kang, *J. Power Sources*, 2005, **142**, 177–183.
167 F. Alcaide, G. Alvarez, J. A. Blazquez, P. L. Cabot and O. Miguel, *Int. J. Hydrogen Energy*, 2010, **35**, 5521–5527.

168 S. Siracusano, V. Baglio, A. Di Blasi, N. Briguglio, A. Stassi, R. Ornelas, E. Trifoni, V. Antonucci and A. S. Arico, *Int. J. Hydrogen Energy*, 2010, **35**, 5558–5568.
169 D. Thirumalai and R. E. White, *J. Electrochem. Soc.*, 1997, **144**, 1717–1723.
170 F. B. Weng, B. S. Jou, A. Su, S. H. Chan and P. H. Chi, *J. Power Sources*, 2007, **171**, 179–185.
171 J. Zeng, B. Jin, P. K. Shen, B. He, K. Lamb, R. De Marco and S. P. Jiang, *Int. J. Hydrogen Energy*, 2013, **38**, 12830–12837.
172 M. Nagao, A. Takeuchi, P. Heo, T. Hibino, M. Sano and A. Tomitab, *Electrochem. Solid-State Lett.*, 2006, **9**, A105–A109.
173 D. A. Boysen, T. Uda, C. R. I. Chisholm and S. M. Haile, *Science*, 2004, **303**, 68–70.
174 J. Zeng, B. He, K. Lamb, R. De Marco, P. K. Shen and S. P. Jiang, *Chem. Commun.*, 2013, **49**, 4655–4657.
175 J. Zeng, B. He, K. Lamb, R. De Marco, P. K. Shen and S. P. Jiang, *ACS Appl. Mater. Interfaces*, 2013, **5**, 11240–11248.
176 T. Tezuka, K. Tadanaga, A. Matsuda, A. Hayashi and M. Tatsumisago, *Solid State Ionics*, 2005, **176**, 3001–3004.
177 Y. Z. Li, E. Muto, Y. Aoki and T. Kunitake, *J. Electrochem. Soc.*, 2010, **157**, B1103–B1108.
178 A. K. Mishra, T. Kuila, D. Y. Kim, N. H. Kim and J. H. Lee, *J. Mater. Chem.*, 2012, **22**, 24366–24372.
179 V. G. Ponomareva, K. A. Kovalenko, A. P. Chupakhin, D. N. Dybtsev, E. S. Shutova and V. P. Fedin, *J. Am. Chem. Soc.*, 2012, **134**, 15640–15643.
180 S. P. Jiang, *Int. J. Hydrogen Energy*, 2012, **37**, 449–470.